Wave impacts on a solid deck in transient wave groups

Hongchao Wang[a,*], H. Santo[a], P.H. Taylor[b], S.S. Dai[c], A.H. Day[c] and E.S. Chan[a,d]

[a]*Technology Centre for Offshore and Marine, Singapore (TCOMS), Singapore 118411, Singapore*
[b]*Oceans Graduate School, The University of Western Australia, Crawley WA 6009, Australia*
[c]*Department of Naval Architecture, Ocean and Marine Engineering, University of Strathclyde, Glasgow G4 0LZ, United Kingdom*
[d]*Department of Civil and Environmental Engineering, National University of Singapore, Singapore 117576, Singapore*

ARTICLE INFO

Keywords:
Extreme wave impact
Focused wave group
Solid deck
I-beam grillage
Entrapped air

ABSTRACT

Wave impacts on an elevated solid deck due to transient focused wave groups are studied numerically. Previously reported experiments with and without an I-beam grillage beneath the deck by Santo et al. (2020) are reproduced successfully in a three-dimensional numerical wave tank based on a two-phase Navier-Stokes solver. The impact loads on the solid deck are relatively simple. The three-dimensional horizontal force, characterised by a single peak in time, is close to two-dimensional, whereas the vertical force consists of upward force and downward suction force. The downward suction force is related to triangularisation of the wetted area underneath the deck and dominated by the added mass effect, which is a three-dimensional effect and therefore any two-dimensional simulation will overpredict the strongly three-dimensional process and the vertical impact loads. The wave impact loads on the solid deck with a grillage are more complicated, with successive force spikes observed for both the horizontal and vertical loads. The significance of entrapped air pockets in the grillage to global wave impact loads is ascertained through interrogating flow field of numerical experiments. It is found that large upward vertical impulsive forces are caused by high local pressures when entrapped down-wave air-pockets are formed, while large downward suction forces are resulted from both high-frequency up-wave air-pocket effect and the low-frequency added mass effect. Large horizontal impulsive forces are due to the combined effects of the down-wave air-pocket and the upward jetting motion of the wave crests. The entrapped air-pocket effects are found to be more important for vertical than horizontal forces.

1. Introduction

Wave-in-deck loads occur when the actual wave crest height exceeds the vertical clearance of a topside deck, and the resultant wave slamming on the deck yields impulsive loading which can be destructive in nature. For existing offshore platforms, the risk of wave-in-deck may increase over the production life due to decreasing instantaneous air-gap (i.e. the difference in elevation between the bottom of the deck and the maximum wave crest). The decrease in air-gap may be associated with settlement of the platforms due to their own weight or seabed subsidence due to decline in pore pressure over the lifetime of hydrocarbon reservoirs, such as the Ekofisk field in the Norwegian part of the North Sea which underwent significant compaction resulting in over four metres of seabed subsidence during 20 years of oil production (Teufel et al., 1991). Meanwhile, with improved statistical estimation of extreme wave crests (Naess and Gaidai, 2011), adoption of a 10^{-4} annual exceedance probability for newer platforms has resulted in an apparent increase in design wave crest height (Scharnke et al., 2017), which leads to the perception that existing platforms may not have adequate air-gaps and may be at risk from significant wave-in-deck loads.

A typical wave-in-deck process is characterised by an approaching wave crest striking the bottom corner of the deck, followed rapidly by a fast jet shooting up the front-face and the remainder of the wave travelling underneath the deck. The initial impact induces large horizontal loads over a short duration due to rapid transfer of fluid momentum. The impact loads are closely related to the approaching wave crest height (or depth of inundation) and crest shape (or water particle velocities underneath the wave surface). Vertical loads on deck comprise an upward slamming force during wave entry stage and a downward inertial force during wave propagation underneath the deck (or wave exit stage).

*Corresponding author
wang_hongchao@tcoms.sg (H. Wang)
ORCID(s): 0000-0003-3933-8896 (H. Wang)

This is a peer-reviewed, accepted author manuscript of the following article: Wang, H., Santo, H., Taylor, P. H., Dai, S. S., Day, A. H., & Chan, E. S. (2022). Wave impacts on a solid deck in transient wave groups. Journal of Fluids and Structures, 114, [103755]. https://doi.org/10.1016/j.jfluidstructs.2022.103755

Present industry design guidelines, such as API (2014) and DNV-GL (2019), rely on empirical formulations to estimate wave-in-deck loads. The horizontal wave impact is approximated following the API method, which is based on a Morison drag formulation (Morison et al., 1950), or alternatively the Kaplan's method, which is based on conservation of momentum (Kaplan et al., 1995). The vertical upward force is estimated either using a drag formulation or Kaplan's momentum method. Since the downward vertical force is dominated by an inertial force resulted from the volume of fluid below the wetted area accelerating downwards, the focus is on accurate prediction of the associated added mass (or the wetted area). Kaplan (1992) approximated the instantaneous wetted area in two dimensions using a simple von Kármán approach, i.e. assuming that the incident wave is not affected by the presence of the deck. Baarholm (2005) extended Kaplan's model to include wave diffraction effects for large volume structures based on the Wagner's approach (Wagner, 1932). While the empirical formulations are widely used during platform design, the accuracy and viability of such an approach are questionable. In reality, wave-in-deck loading is much more complicated with possible dependence on the approaching wave crest height and crest shape, as well as entrapped air, air compressibility, and so on.

Recent progress in characterising wave-in-deck loads can be seen from the recent experimental work by Scharnke et al. (2017) and Ma and Swan (2020b). The dependency of horizontal impact load on inundation level and horizontal water particle velocity at crest is observed via two-dimensional (2D) and three-dimensional (3D) wave-in-deck tests, respectively. Sivagamasundari and Sannasiraj (2020), Park et al. (2017) and Fang et al. (2021) investigated experimentally the effect of clearance/air-gap on wave-in-deck loads on a horizontal plate, a box-shaped model and a coastal bridge model with underneath girders, respectively. Numerical simulations based on Navier-Stokes solvers show promise in predicting wave-in-deck loads and similar problems. Chen et al. (2018) numerically reproduced the 2D wave-in-deck experiment conducted by Kendon et al. (2010), and the simulated horizontal and vertical impact forces on a deck using a Stokes fifth-order wave seem to match well with the measured forces from the first wave impact. Hayatdavoodi et al. (2014) simulated impact forces on a coastal bridge deck with girders due to solitary waves, and the agreement between numerical results and experimental data for horizontal and vertical forces is generally good for the submerged deck. However, the numerical results show larger discrepancies when the deck is elevated, highlighting the potential challenge of accurate prediction of vertical impact loads due to wave-in-deck. Lind et al. (2015) and Sun et al. (2019) employed smoothed hydrodynamics method to study 2D wave-in-deck loads and horizontal plate impact onto a wave crest and flat water surface, respectively, emphasising the importance of including the air phase for accurate simulations of impact problems. Recently, Ma and Swan (2020a) introduced a new model, Lagrangian Momentum Absorption (LMA) scheme, to predict horizontal wave-in-deck loads based on conservation of momentum formulated in a Lagrangian frame of reference. The new analytical model represents a significant improvement over existing analytical methods without the use of empirical coefficients. Nevertheless, accurate prediction of vertical impact loads remains a challenge.

Part of the challenge in modelling vertical loads accurately is due to trapped/entrapped air pockets. The role of entrapped air is an important consideration for reproducing wave impact pressure, as demonstrated recently by Bredmose et al. (2009) using a novel 2D compressible aerated-flow solver and Liu et al. (2019) making use of a 2D compressible viscous flow solver. The effect of entrapped air can be seen through the emergence of high pressures propagating away from the impact zone in a form of a hemispherical pressure wave which can develop into a shock wave (Dias and Ghidaglia, 2018). However, the role of entrapped air and air compressibility for overall impact forces are less discussed in the context of wave-in-deck, and much of the focus is on wave impact on coastal bridges and jetties due to recent examples of significant damage in hurricanes, see for instance Cuomo et al. (2009); Hayatdavoodi et al. (2014); Azadbakht and Yim (2016), among others. In general, entrapped air effect is found to be responsible for increasing vertical wave impact loads. The effect of air compressibility, on the other hand, is found not important for the overall forces on a bridge with underneath girders, as shown by solving models with both incompressible and compressible Euler's equations (Seiffert et al., 2015). The cushioning effect of entrained air (dispersed as small bubbles in water rather than a large entrapped air-pocket) on violent wave impact was investigated by Peregrine and Thais (1996) and Bredmose et al. (2015). With the joint action of wind and wave, the wave-deck interactions with entrapped air-pockets can become even more complex (Liu et al., 2022; Wen et al., 2022).

Existing numerical studies on wave-in-deck are mostly 2D and concerned with parametric studies, with rather few paying attention to the physical details of wave-deck interactions, as well as the effects of entrapped air on the overall forces. In light of the above, this paper aims to reproduce 3D wave-in-deck loads measured on a solid deck structure by Santo et al. (2020). In that set of experiments, the effects of the presence of I-beam grillage mounted underneath the deck were also examined altogether. Deterministic focused wave events (Tromans et al., 1991) based upon a realistic

Fig. 1: (a) Photograph of the overall setup and the towing tank. (b) Close-up view of the deck model, here shown rotated at 45° relative to the wave direction.

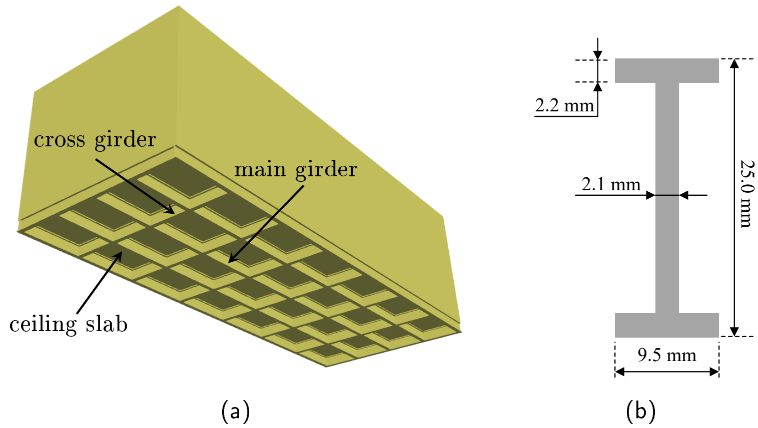

Fig. 2: Illustration of the (a) overall shape and (b) cross section of I-beam grillage mounted underneath the deck.

JONSWAP spectrum was used as a good representation of the largest waves arising in realistic sea-states. For wave-in-deck, the use of focused wave group allows better control of the kinematics of a transient incident wave group interacting with the deck. Subsequently, the focus of this paper is on analysing the complex 3D wave-deck interactions by interrogation of flow field details, as well as on investigating the role of entrapped air on the global wave-in-deck loads.

The paper opens with a brief introduction to the experiments (§2), followed by the description of the numerical set-up (§3). The experiments of wave-in-deck loads for deck without and with an I-beam grillage are reproduced in §4 and §5 successively, and the wave-structure interactions are investigated in detail. The effects of air entrapment are investigated in §6. Finally, some conclusions are drawn.

2. Experimental set-up

The experiments by Santo et al. (2020) were conducted in the towing tank of the Kelvin Hydrodynamics Laboratory at the University of Strathclyde, Glasgow. Although full details of the experiments are given in that paper, we provide a brief summary of the experimental tests. The towing tank is 76 m in length, 4.6 m in width and operates with a water depth of 1.8 m. A four-flap absorbing wavemaker is mounted at one end for wave generation and a sloping beach at the other end for wave absorption. In the experiments, a solid deck model with length L, width B and height H of 1.05

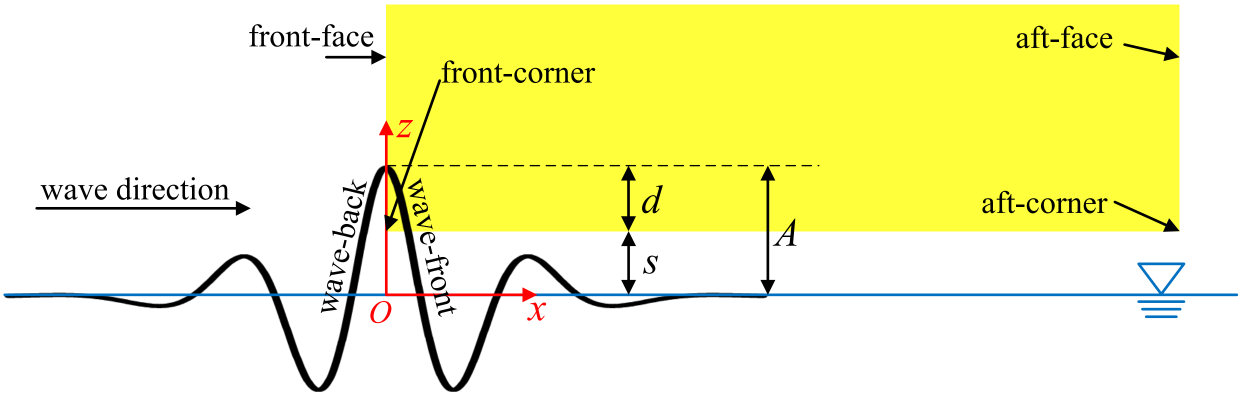

Fig. 3: Definition sketch of the wave-in-deck problem.

m, 0.4 m and 0.3 m, respectively, was suspended rigidly below a heavy carriage held stationary and spanning the tank through a 6 degree-of-freedom force/moment transducer providing a stiff single point support for the deck model.

Fig. 1 provides photographs showing the overall setup of the experiments and a close-up view of the deck model which was rotated to 45° relative to the wave direction (for improved visibility in the photographs). Underneath the solid deck, an I-beam grillage could be mounted to represent support beams on a large second generation North Sea platform. Fig. 2(a) shows the overall shape of the I-beam grillage. A total number of 8 I-beams (or 'cross girders') span the length of the deck with 7 spacings between them, the first and last at the ends being 14.5 cm wide and the central five being 15.2 cm wide. Along the axis perpendicular to the wave propagation direction, 5 I-beams (or 'main girders') are regularly spaced with 4 equal spacings of 10 cm between them. The ceiling slabs are the deck bottom formed by the main and cross girders. As shown in Fig. 2(b), the cross section of the I-beams consists of two flanges of 9.5 mm in width and 2.2 mm in height, connected by a web of 2.1 mm in width and 20.6 mm in height, so the total length of each I-beam is $I = 25$ mm.

Fig. 3 shows the definition sketch of the wave-in-deck problem. The coordinate system is defined with x axis pointing towards the wave propagation direction, z axis pointing vertically upwards and y axis following the right-hand rule. The origin O is right under the front-face of the deck and at the still water level, and $y = 0$ passes through the mid-plane of the deck. The solid deck was placed at $s = 21$ cm above still water level. The orientation of the structure was 0° (referred to as 'head-on' direction) so that the long-side of the structure was aligned with the wave propagation direction. Transient wave groups were used as the incident waves, based on a JONSWAP spectrum with peak frequency of 0.52 Hz and zero-crossing period of $T_z = 1.8$ s. The wave groups were made to focus at the leading-edge (or front-face) of the solid deck, with a nominal crest amplitude of $A = 25.6$ cm at the focus location. The free-surface elevation was measured by a resistance-type wave probe mounted from the towing carriage midway between the leading edge of the deck model and the side of the tank with a sampling rate of 3571 Hz, while the horizontal and vertical forces on the structures were recorded by a 6 DOF force transducer (Kistler 9257B) at the same sampling rate as the wave probe. The weight of deck in air was recorded in the measured vertical loads before conducting the experiments, so the force measurements reported throughout are solely due to the incident waves. In this paper, we consider two scenarios: wave impact on a solid deck without and with an I-beam grillage. In the latter scenario, the deck was elevated by 25 mm and the I-beam grillage was attached underneath the deck, achieving the same inundation level of $d = 4.6$ cm as in the solid deck only scenario.

Although this paper aims at reproducing the violent wave-in-deck events from the laboratory-scale experiments, it is worthwhile to define appropriate scalings for quantities of interest from the laboratory to the field. We assume a laboratory to field Froude length scaling of 1:80 consistent with a large platform in the central/northern North Sea. Then the deck dimensions become 84 m long, 32 m wide and 24 m high, and the I-beams are 2 m high. The undisturbed wave crest is 20.5 m above mean-sea-level on a water depth of 144 m, and the distance from the still water level to the bottom of the structure (i.e. deck bottom for the solid deck only case and I-beam bottom for the solid deck with grillage case) is assumed to be 16.8 m. Here, we examine only the zero current case, though experiments were performed with a full-scale in-line current of 1.25 and 2.5 m/s as well. Of course, we recognise that scaling of impact forces and in particular pressures is somewhat difficult due to possible surface tension, bubble properties and air compressibility effects. However, Froude scaling at least provides a starting point for comparing loading behaviour between the towing tank and the field. With Froude length scaling of 1:80, this applies to all physical lengths: deck geometry, depth of inundation, water depth, wave height and wavelength etc. Timescales vary as $1 : 80^{0.5} \sim 9$, forces as $1 : 80^3 \sim 0.51 \times 10^6$ (so a force of 1 N on the model in the tank becomes 0.51 MN on the platform in the field), and momentum/impulse as $1 : 80^{3.5} \sim 4.6 \times 10^6$.

3. Numerical set-up

The experiments are reproduced in a fully nonlinear numerical wave tank (NWT) established based on the OpenFOAM scheme with the toolbox 'waves2Foam' (Jacobsen et al., 2012) for wave generation and absorption. The governing incompressible Navier-Stokes equations in Eulerian coordinates are solved using a finite volume method without use of any turbulence models. The interface between air and water, the free-surface, is tracked using a modified volume of fluid (VOF) approach (Berberović et al., 2009), wherein an indicator function $\alpha \in [0, 1]$ is used to represent the volume fraction of water: 0 for air, 1 for water and values in-between representing a mixture of both phases. Surface tension is not represented numerically, since the Bond number $B_o = gL^2\Delta\rho/T_s \simeq 1.5 \times 10^5$ (where g is gravitational acceleration; $\Delta\rho$ is the difference in density of the two phases; $T_s = 0.073$ N/m is the surface tension). This is well above the range where surface tension is important, according to Faltinsen and Timokha (2009).

A relaxation zone is applied at the down-wave end of the NWT to ensure the propagating waves are absorbed properly. Other boundary conditions include a velocity inlet boundary condition for wave generation, a 'pressureInletOutletVelocity' boundary condition at the top of the NWT allowing entry and exit of air, symmetry boundary conditions at the side-walls of the NWT, and no-slip boundary conditions for the deck box.

To save computational cost, the length of the NWT was reduced to $4.6\lambda_p$ and the focus point was set at $1.6\lambda_p$ away from the inlet boundary (here λ_p=5.5 m is the peak wavelength). The width of the NWT was chosen as $5B$, so the distance from either side of the deck to the side-wall of the NWT is $2B$. This is large enough because the scattering of the waves sideways out from the deck is mainly within $0.5B$, as observed from experimental videos. The NWT was $10H$ in height, and the water depth was $6H$ (same as in the experiments).

To account for the difference caused by the change of focus location in the NWT, an iterative method was employed to re-create the experimental incident wave signal recorded at the focus point (see details in Wang et al. (2018) and Vyzikas et al. (2015)). As wave impact on deck is closely associated with both the inundation level and the crest shape of incident wave, it should be emphasised that accurate reconstruction of the experimental incident wave is essential for successful reproduction of wave-in-deck experiments. During the iteration process, the following factors made the re-creation very challenging:

- The importance of accurate inundation level imposes a more stringent standard of performance for incident wave re-creation. This is especially true when the inundation level is small compared to the incident wave height, e.g., an incident wave with nominal wave amplitude only 1 cm (or 4%) smaller than the desired value of 25.6 cm means a difference of 22% for a 4.6-cm-inundation and 48% for a 2.1-cm-inundation. Previous numerical studies on wave-in-deck problems seem not to have emphasised the importance of this 'small' difference.

- Even when the time series and amplitude spectra of incident waves are almost the same, the local details of the wave crest can be different (e.g. symmetric, overturning or breaking) leading to different impact loads.

- As the incident wave signal is very steep and close to breaking, undesired breaking may occur during the iteration process and thus destroying the applicability of the iterative method.

- In the experiments, the wave probe was mounted at a single point transversely midway between the side-face of the deck model and the side-wall of the tank, so how uniform the wave crest across the tank width is important. This may induce some difference in elevation along the nominally constant elevation crest in the experimental towing tank.

In view of the above, considerable effort was made to re-create the experimental incident wave with the closest inundation level while avoiding wave breaking or overturning, which did not occur in the experiments.

The NWT is discretised on a structured mesh. The choice of mesh size is determined by convergence tests with details outlined in the Appendix A. For the optimum mesh, the streamwise mesh size along the wave propagation

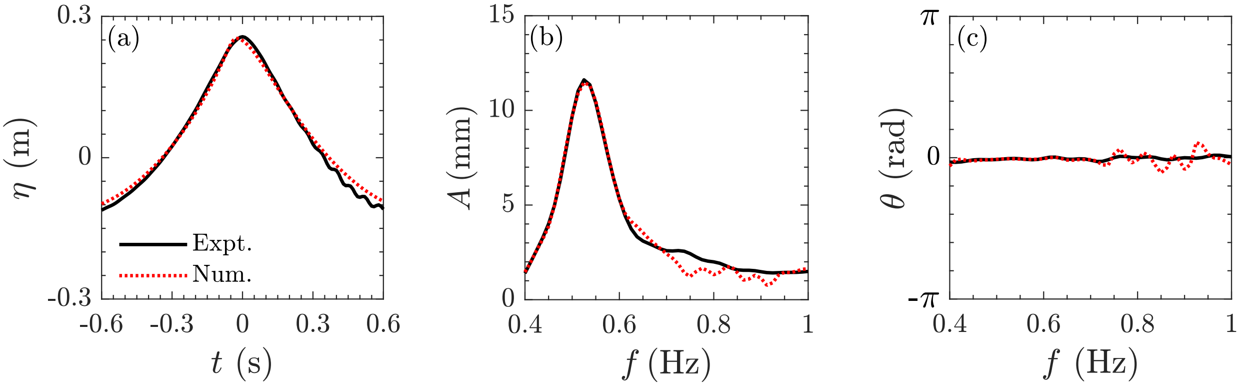

Fig. 4: Comparison of experimental and numerical incident wave (a) time history near focus time (b) amplitude spectrum and (c) phase spectrum. The numerical incident wave is simulated without the presence of the deck model.

direction in the upstream is chosen to achieve ~550 cells per peak wavelength to resolve propagating incident waves, and is gradually reduced to ~2200 cells per peak wavelength in regions around the front-face of structure; the vertical cell height near the free-surface is chosen to give ~200 cells per nominal wave height ($2A$) to capture wave motions; the transverse mesh size is chosen to have ~730 cells per peak wavelength. A typical simulation with the optimum mesh has a total cell number of 67.9 million and requires approximately 0.03 million CPU hours, computed using 720 cores on a supercomputer with 2.6 GHz Intel Xeon E5-2690 v3 CPUs. For robustness and convergence, the time step of the simulations was chosen to be runtime adaptive with maximum Courant number not exceeding 0.5.

Using the optimum mesh and numerical settings the incident wave group is re-created with good accuracy as shown in Fig. 4, where $t = 0$ s corresponds to the instant of the maximum experimental wave elevation recorded at the focus point. This wave group will be used for the subsequent 3D simulations to obtain the impact loads on solid deck without and with an I-beam grillage.

The horizontal and vertical wave-in-deck loads are calculated as a sum of pressure and viscous forces in corresponding directions, which are obtained by summing up normal pressures and shear stresses over all surfaces of deck, respectively. The recorded vertical wave-in-deck load excludes the initial upward buoyance force on the deck arising from the air pressure difference between the bottom and top of deck before comparison with the dynamic pressure measurements (i.e. the force transducer loads with the static weight of the box removed).

4. Wave-in-deck loads on a solid deck

Fig. 5 provides the comparison of force time histories for wave impact on a solid deck without an I-beam grillage (referred to as 'case A'). The measured forces are shown as solid black lines while the numerical results are shown as dashed red lines. It can be seen that the measured horizontal force consists of a single peak in time, followed by oscillation due to structural resonance as reported by Santo et al. (2020). Meanwhile, the measured vertical force consists of both upward and downward (suction) phases in time as the wave propagates below and around the deck, and the structural resonance is less pronounced. The numerical results do not contain the structural resonance, and relatively good agreement can be observed for both force time series, although the magnitude of the first upward vertical peak force is underpredicted by 20%. Applying a low-pass filter to both time series with a cut-off frequency of 9 Hz produces a comparison with much better agreement, as shown in Fig. 6. The slight phase lag apparent from the comparison of the horizontal peak force is removed after the filtering. Such a phase lag due to structural dynamics is consistent with the experimental observation of plunging wave forces on a vertical wall by Chan and Melville (1989). Nevertheless, the underprediction of the first upward peak force still exists even after filtering.

It is interesting to note an obvious second peak in the vertical force time series of both experimental and numerical results, which is a robust feature and also present in previous experiments (Kendon et al., 2010; Abdussamie et al., 2017; Sivagamasundari and Sannasiraj, 2020; Duong et al., 2021) and numerical studies (Wu et al., 2016; Chen et al., 2018). However, no explanation was given in these studies. Recently, Duong et al. (2022) attributed the presence of the local peak to the vortex that occured when the wave receded from the deck, based on the velocity field and estimated

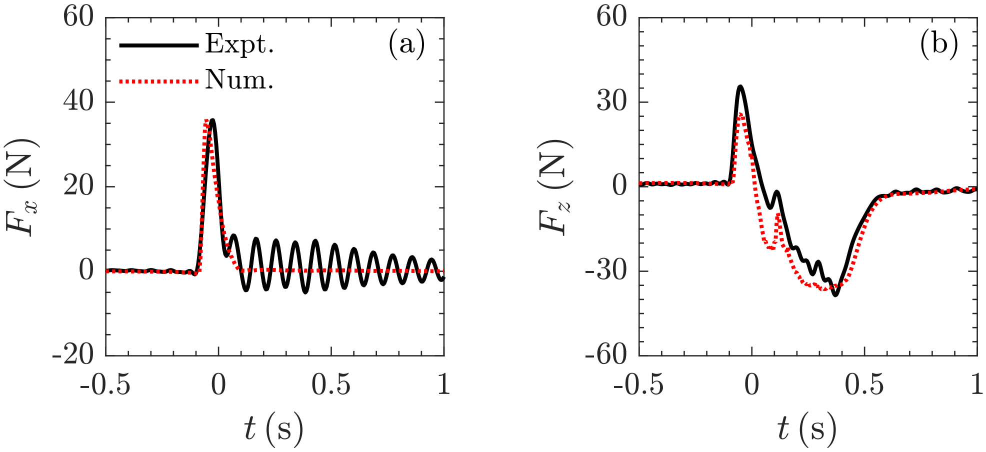

Fig. 5: Time series of (a) horizontal force and (b) vertical force on structure for solid deck without an I-beam grillage.

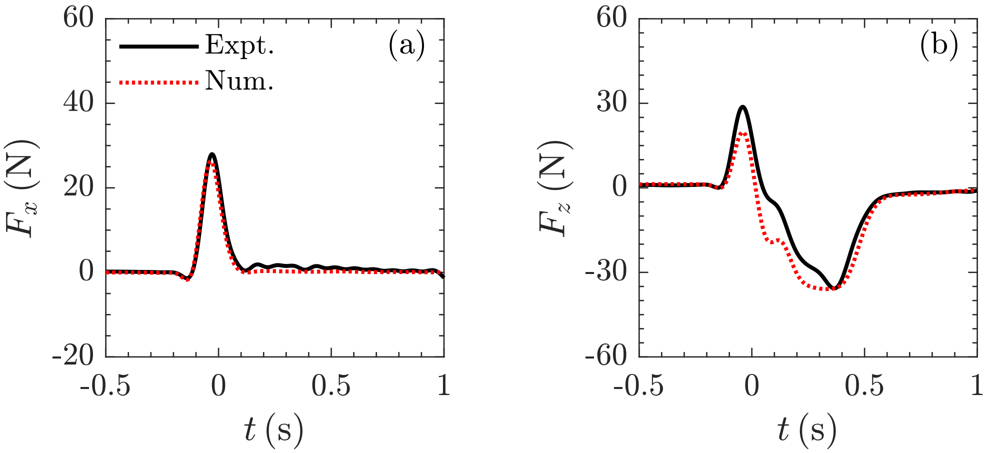

Fig. 6: Time series of low-pass filtered (a) horizontal force and (b) vertical force on structure for solid deck without an I-beam grillage. The cut-off frequency of low-pass filter is 9 Hz.

pressure distribution obtained from their particle image velocimetry results. In contrast, we will demonstrate shortly that the occurrence of the second peak is caused by the wave-back slamming on the underside of the deck as the incident wave drops below the front-edge of the deck.

The following definitions are made to facilitate the description of the flow field. The bottom corner and the vertical face of the deck towards the wave paddles can be described as the front-corner and front-face, respectively, and those towards the absorbing beach as the aft-corner and aft-face, respectively, see Fig. 3. The definitions of wave-front and wave-back are also shown on this figure. The wave underneath the deck is referred to as the 'under-deck' wave, while the wave transversely between the side-faces of the deck and the side-walls of the tank is split into the 'near-field' close to the deck box and the 'far-field' out towards the tank walls, respectively. Note that the snapshots of the free-surface and the pressure contours on the deck will be presented at the same time instants in the following sections, to better relate the wave-deck interactions to various aspects of the flow field.

Fig. 7 shows the time series of free-surface elevation and forces on the deck in the same figure, where the vertical position of the deck bottom, $z = s$, is indicated using a horizontal dashed grey line. From the points of intersection between the deck bottom line and the time series of the incident wave (approximately $t_1 = -0.08$ s, $t_2 = 0.07$ s), two vertical dashed grey lines are drawn to characterise the time interval of interaction, which is referred to as the 'wave entry' stage. This stage involves the wave-deck interaction from the initial contact of the wave-front with the

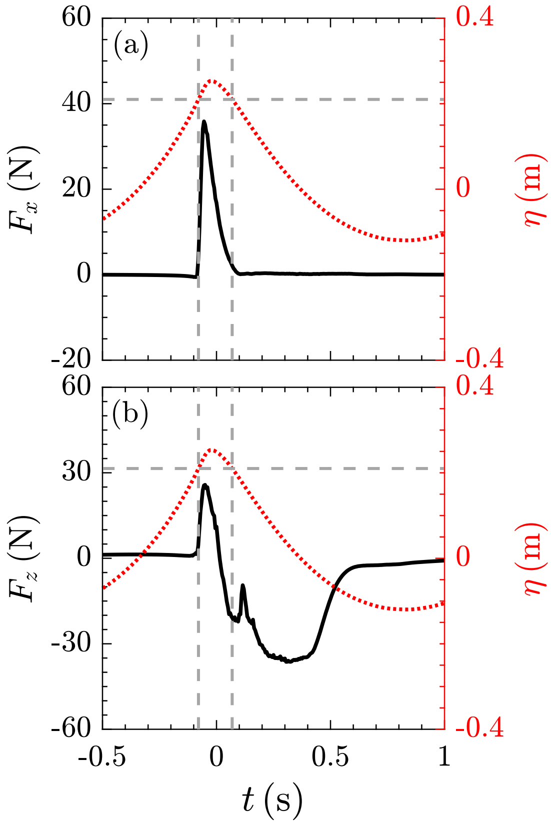

Fig. 7: Time series of numerical incident wave group and forces on structure for solid deck without an I-beam grillage. Solid black lines for (a) horizontal force (b) vertical force; dotted red line for incident wave.

deck front-corner to the wave-back dropping below the deck front-corner, or leaving the deck front-face, defined in terms of the motion of the undisturbed water surface through these positions. The second stage, referred to as the 'wave propagation' stage, is defined as the period after the 'wave entry' stage, including a local slamming at the deck bottom immediately after the wave-back leaves the deck front-face, and wave propagation underneath the deck followed by water exit, either by dropping away from the bottom of the box or by reaching the far aft-end of the box. Obviously, the horizontal force of interest is only present during the wave entry stage, while the vertical force of interest covers both stages.

To gain an overall insight into the wave-in-deck process, the evolution of free-surface during wave-deck interaction is shown in supplementary Movies 1-3 from different views (available at xxxx), and the corresponding snapshots are shown in Fig. 8 to Fig. 10, respectively. The free-surface is extracted by choosing the indicator function $\alpha = 0.5$. This is reasonable since for cells with $\alpha < 0.5$ the volume of water is considered small, so they are relatively unimportant in understanding the general process of wave-structure interaction, while removal of $\alpha > 0.5$ is desirable for clearer visualisation. In this way, it should be noted that only the interface between water and air is shown and cells with $0.5 < \alpha \leq 1$ are not displayed in the movies. Consequently, although at some moments a portion of deck surface is apparently not covered by water (i.e. the exposed yellow region) in the movies, it is actually fully wet with no entrapped air-pockets ($\alpha = 1$). For Movie 3 and Fig. 10, the free-surface $\eta \geq s$ is indicated using red colour. In this way, the propagation of the main wave event outside the deck and the boundaries of jets formed underneath the deck can be identified.

The wave entry stage commences from $t = -0.08$ s and ends at $t = 0.07$ s. Part of the wave crest strikes head-on with the front-face of the deck while the remaining wave advances along the deck bottom. Due to incident wave impingement on the front-face of the deck, a jet quickly shoots vertically upwards, forming a thin layer or sheet where the water motion is very close to 2D with only a localised wrap-around at the vertical corners of the box, as shown in

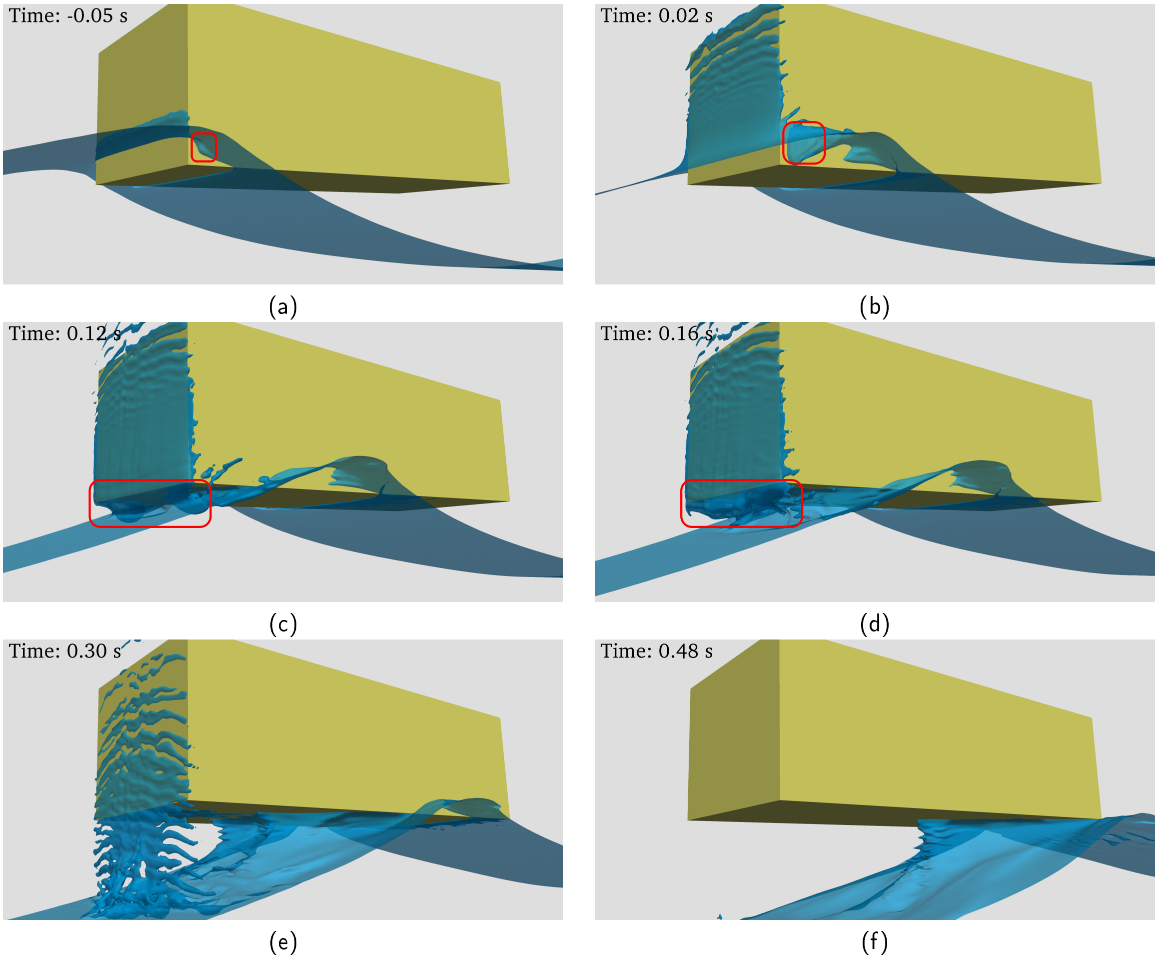

Fig. 8: Evolution of free-surface from side view for solid deck without an I-beam grillage. The red boxes are used to facilitate discussion.

Fig. 8(a) and (b), and also in figure 10 in Santo et al. (2020). It is therefore reasonable to assume that all the incident horizontal momentum of the fluid is lost and the impact drives the vertically moving sheet and hence the high but short horizontal impact force time series on the deck is observed.

When the wave impinges on the front-face of the deck, the horizontal force is induced due to the very rapid change in fluid horizontal momentum. Fig. 11 shows the snapshots of pressure contour at the front-face at $t = -0.05$ s and $t = -0.02$ s. Combining this with Fig. 7 and Fig. 9, it is found that the horizontal force reaches its maximum at $t = -0.05$ s, preceding the occurrence of the maximum elevation of the undisturbed incident wave which gives the largest inundation at $t = -0.02$ s, due to the slightly inclined wave crest to the wave propagation direction. This suggests that the impact force is not solely dependent on the depth of inundation. Other factors such as the crest shape (specifically the angle between the wave-front and the front-face of the deck for non-overturning and non-breaking waves) and the associated velocity profile underneath the crest can be important as well. Interestingly, the impact pressure is uniform across the surface. There are some edge effects, particularly at the bottom corners of the front-face of the box (note the fine grids at the front-face in Fig. 11(a) are able to capture the edge effects), but overall the impact pressure is close to uniform. Fig. 12 further demonstrates that the pressure distributions recorded at different vertical positions of the front-face are close to uniform across the width except near the edges. Given this, a 2D simulation that has a longitudinal slice of the deck model with configuration otherwise the same as the 3D wave-in-deck simulation is found to give a good estimate of the 3D horizontal impact force, with details outlined in Appendix B.

To investigate the nature of vertical impact force, Fig. 13 shows snapshots of pressure contours on the underside of the deck, with Movie 4 attached in the supplementary material. During the initial phase of wave entry, the wave

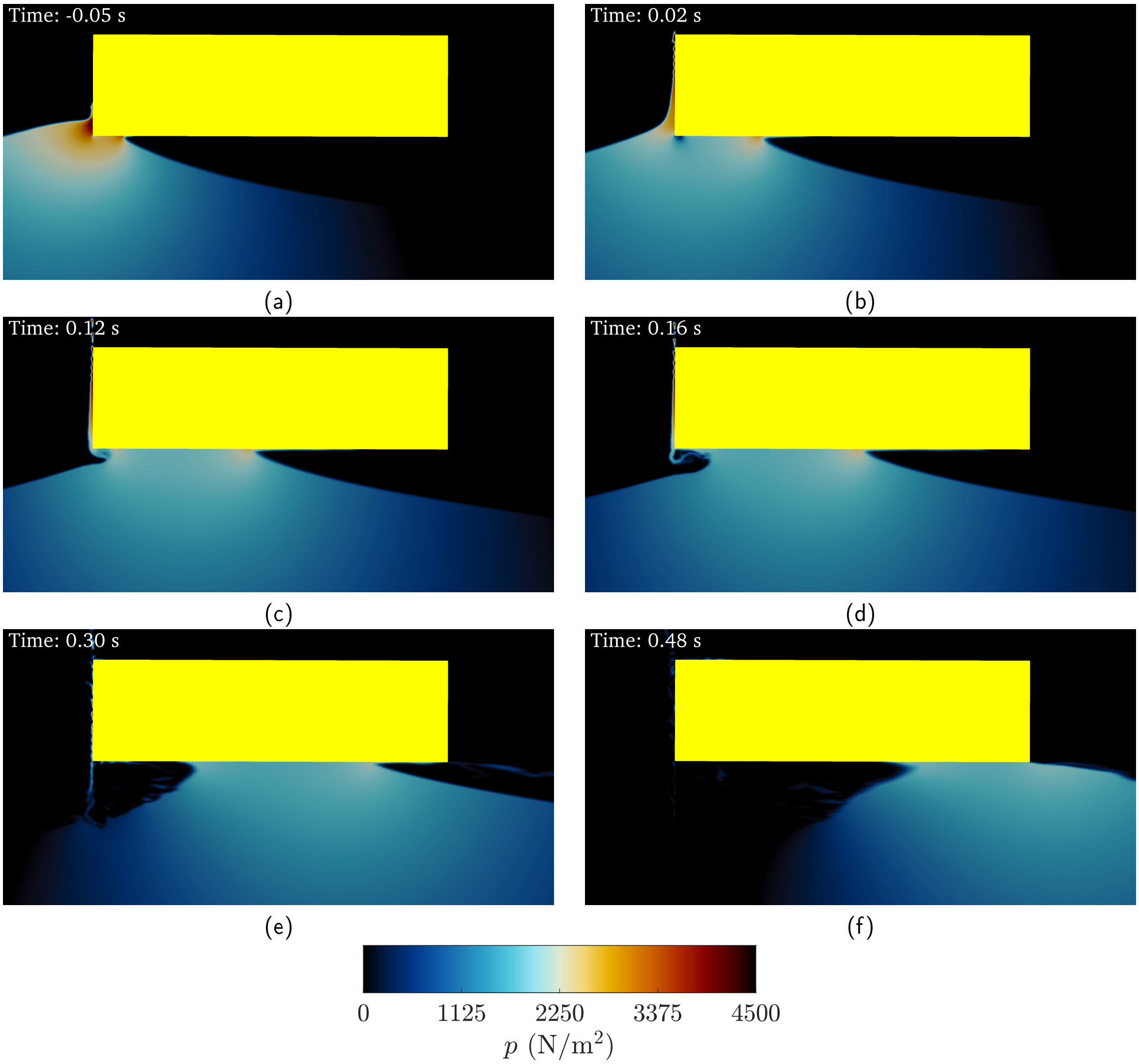

Fig. 9: Pressure of flow field from side view on a vertical sheet at $y = 0$ (the centre-line along the tank and through the box) for solid deck without an I-beam grillage.

exerts an upward pressure on the deck as it collides with the deck bottom due to the upward vertical velocity under the wave-front crest and buoyancy change. The region of positive pressure gradually develops in length and becomes largest at $t = -0.05$ s, as shown in Fig. 13(a), which corresponds to the occurrence of the largest upward vertical force. From $t = -0.04$ s onwards, a region of negative pressure (corresponding to a leading region) starts to develop in length over time near the front-corner of the underside of the deck, and hence the vertical force on deck starts to decrease. At $t = 0.02$ s as shown in Fig. 13(b), the pressure contour gradually varies from positive pressure at the leading region to negative pressure towards the front corner of the deck. At this time instant, the vertical force is turning into a downward suction force (pressures being below the atmospheric pressure).

The wave propagation stage commences as the wave-back starts to drop below the deck front-corner at $t = 0.07$ s. The water sheet at the front-face of the deck continues its run-up due to inertia. The bottom part of the water sheet (near the front-corner) is 'stretched' from the front-corner towards the wave-back as the wave advances further away from the front-face, which then gets separated around $t = 0.15$ s (see the red boxes in Fig. 8(c) and (d), and Movie 1). In the meantime, the wave surface wrapping around the side-faces of the deck (see the red boxes in Fig. 8(a) and (b)) develops towards the deck bottom and interacts with the 'stretched' water sheet, leading to the formation of a large 'chunk' of water near the front-corner (see Fig. 8(d) and Fig. 10(d)). The 'chunk' of water near the front-corner and the

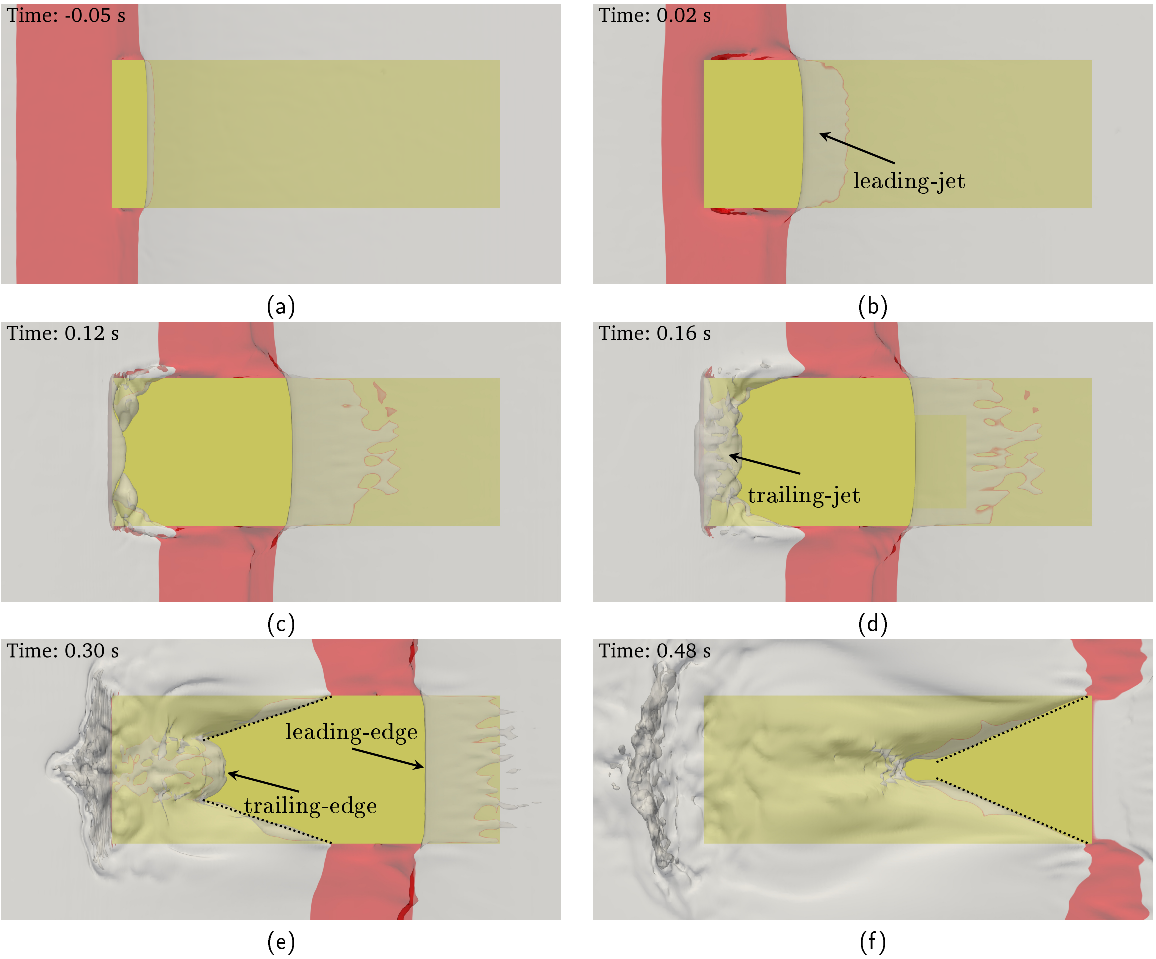

Fig. 10: Evolution of free-surface from bottom view for solid deck without an I-beam grillage. The incident wave propagates from left to right; red color and grey color represent free-surface above ($z \geq s$) and below the deck bottom ($z < s$), respectively; the exposed yellow region represents the fully-wetted area of the bottom of the deck box; the dotted black lines in (e) and (f) illustrate the triangularisation of the wetted area.

water sheet above the front-face simply fall into the water below the deck, leading to the formation of a water-curtain (see Fig. 8(e) and note that $\alpha < 0.5$ is not shown therein). This is also observed in the experimental snapshot as shown in Fig. 16.

Meanwhile under the deck, a local positive pressure region quickly develops as the wave-back leaves the front-corner and drops below the deck. The positive pressure region starts to increase from around $t = 0.1$ s, becomes largest at $t = 0.12$ s as shown in Fig. 13(c), and quickly disappears, thus behaving as a close to impulsive slamming force. These all correlate well with the presence of the second peak in the downward vertical force time series. As the wave-back slams on the underside of the deck near the front-corner, a 'trailing-jet' (see Fig. 10(d)) is formed behind the wave-back at the deck bottom, which is stretched as the wave propagates down along the deck, and quickly destroyed leaving a smaller sheet of water travelling with the wave (see Fig. 10(e)).

The largest downward vertical force occurs during the stage of wave propagation under deck, which is at $t = 0.30$ s. Fig. 10(e) shows the bottom view of the free-surface at this time instant, where the outlines at the leading and trailing sides of the fully wetted region under deck (i.e. yellow region) are referred to as 'leading-edge' and 'trailing-edge', respectively. Triangularisation of the fully wetted region following the wave crest is observed as the wave crest propagates down-wave across the underside of the deck – the leading-edge remains almost straight across the deck width while the trailing-edge contracts from the sides to the middle (see Fig. 10(e) and (f)), gradually forming a 'V' shape as the wave exits the aft-face of the deck (see Fig. 10(f)).

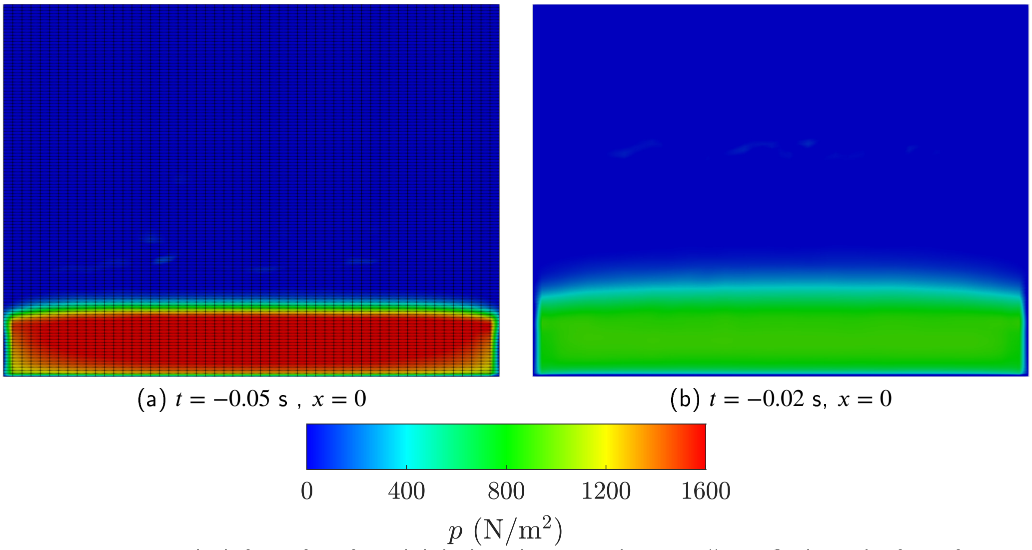

Fig. 11: Pressure contour on deck front-face for solid deck without an I-beam grillage. Grids at the front-face are illustrated in (a).

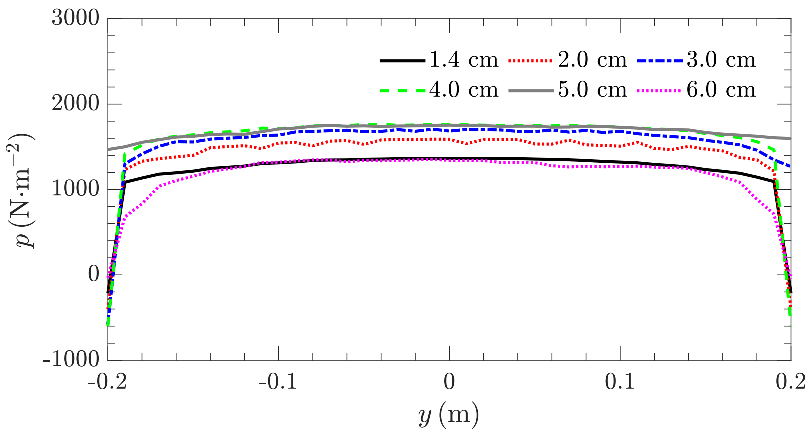

Fig. 12: Pressure distribution across the width of the front-face at different vertical positions for the deck only case at $t = -0.05$ s. The sampling positions in the legend are measured vertically upwards from the deck bottom.

Looking at the corresponding variation in the pressure contour, Fig. 13(e) shows that the wetted area consists of a close-to-planar leading region of positive pressure weakening during wave passage down-wave the deck, followed by a bulk suction zone with the negative pressure being largest at the centre and decreasing outwards along the radial direction. During the wave propagation under the deck, the fully wetted area increases in size from $t = 0.12$ s to $t = 0.23$ s, remains almost unchanged from $t = 0.23$ s to $t = 0.40$ s and quickly decreases as the wave starts to exit the aft-face of the deck from $t = 0.41$ s. This is consistent with the trend in the force time series shown in Fig. 7(b) – the downward vertical force experiences a swift increase from $t = 0.12$ s to $t = 0.23$ s, a slight lull with variation as large as 5% of the largest downward vertical force from $t = 0.23$ s to $t = 0.40$ s and a rapid decrease from $t = 0.41$ s onwards. This illustrates that the downwards 'suction force' is closely related to the wetted area under the deck (and accordingly the associated added mass). Since the triangularisation of the fully wetted region is a 3D effect, 2D simulations of wave-in-deck will overestimate the vertical suction force, consistent with the finding of Baarholm (2009).

Fig. 14(a) shows the impact pressure time series calculated at the front-face. The sampling points are located at 2 cm and 3 cm above the deck bottom and right in the middle of the front-face (i.e. $y = 0$). The pattern of pressure is simple with a single large peak in time, similar to the pattern of wave impact pressure on a vertical suspended wall

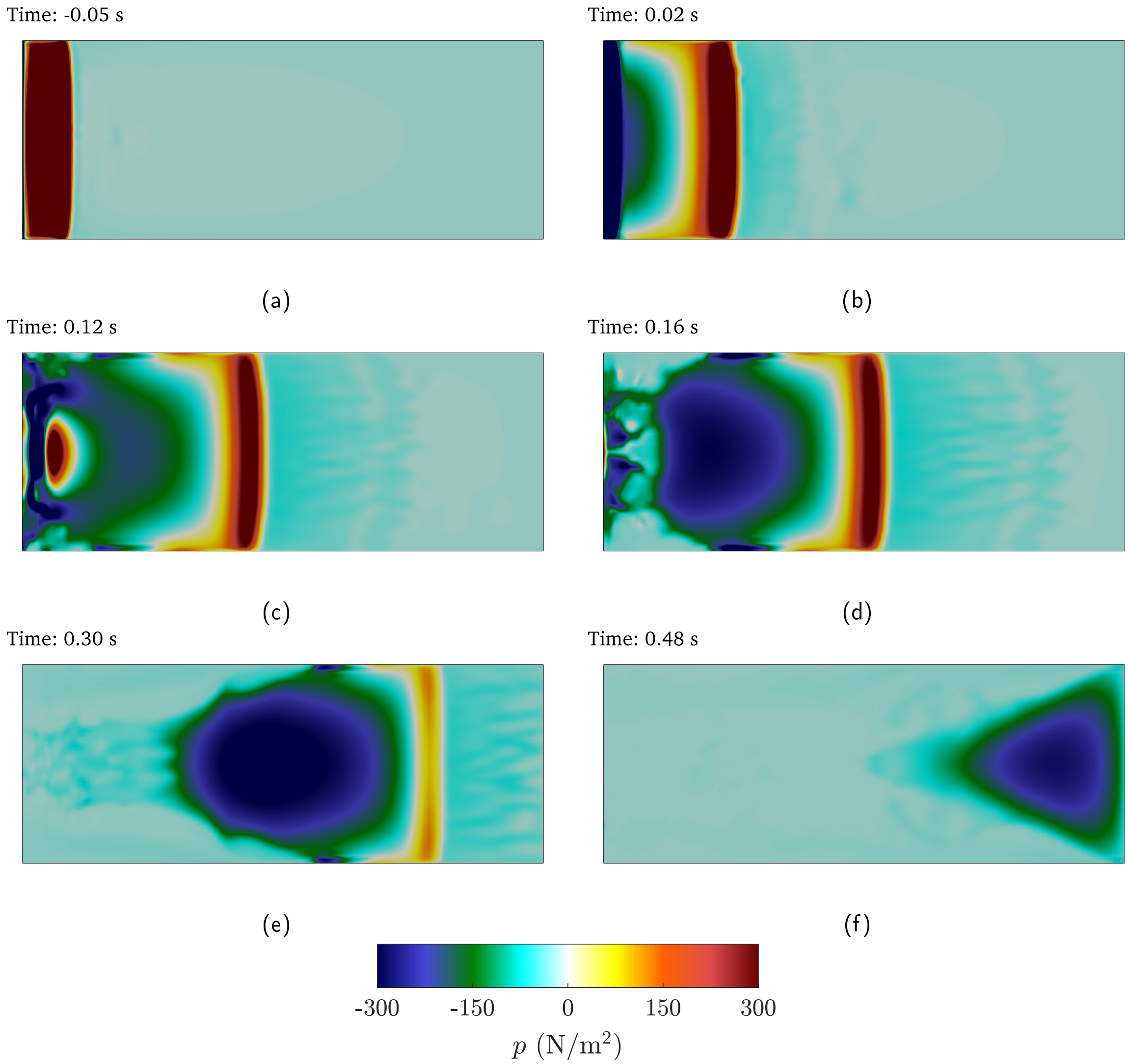

Fig. 13: Evolution of pressure on the underside of the deck for solid deck without an I-beam grillage.

in the absence of air entrapment presented in Hattori et al. (1994). Fig. 14(b) shows the impact pressure time series calculated at the sampling points along the deck bottom and $y = 0$. The first positive peak of the pressure time series is related to the leading region of positive pressure propagating down the deck bottom, while the second positive peak of pressure at $x = 6$ cm is due to the wave-back slamming at the deck bottom as explained above. In particular, a much larger negative pressure peak is found at the deck bottom near the front-corner, i.e. $x = 2$ cm. As shown in the pressure and vorticity contours captured at $t = 0.08$ s in Fig. 15, this is induced by the negative pressure region formed in the fluid underneath the front-corner, which is associated with the vortices generated therein as the wave-back drops below the sharp front-corner.

5. Wave-in-deck loads on a solid deck with an I-beam grillage

Wave loads on the same deck but with an I-beam grillage underneath (see Fig. 2, referred to as 'case B') were simulated with the same inundation of $d = 4.6$ cm. Fig. 17 shows the measured time series of horizontal and vertical loads on the structure (solid black lines). Both force time series are characterised by sharp peaks with high frequency oscillations in time, indicating that the measured force time series are more affected by structural resonances than the deck only case. From the comparison with the simulated forces (dashed red lines), it can be seen that in general the level

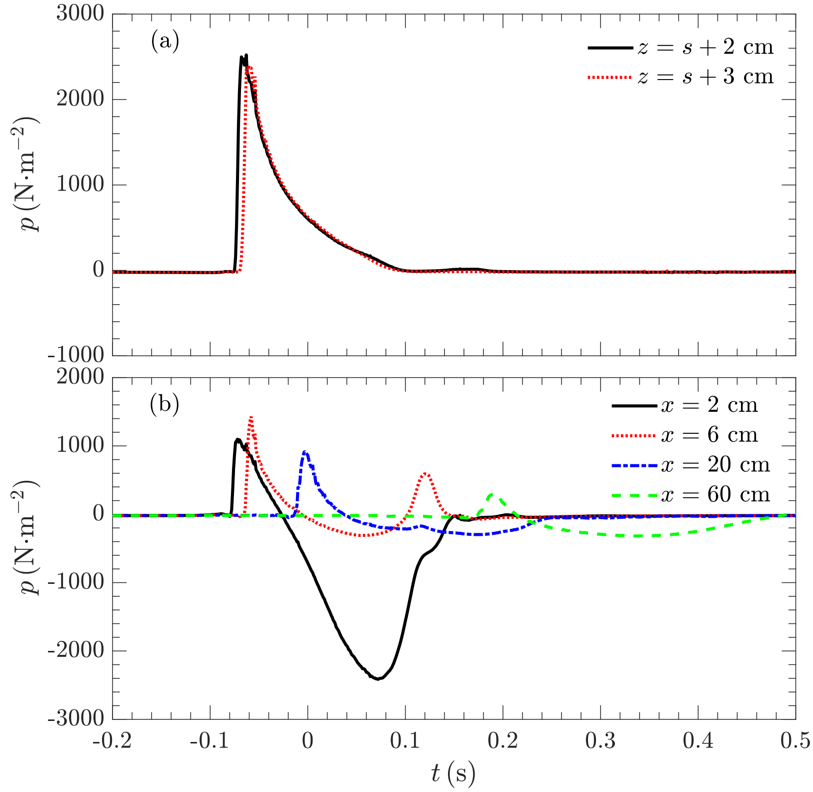

Fig. 14: Time series of pressure calculated at the deck (a) front-face and (b) bottom for the solid deck only case. The vertical sampling positions in (a) are 2 cm and 3 cm above the deck bottom; the longitudinal sampling positions in (b) are the distance down-wave from the front-face; the transverse position of the sampling points is $y = 0$.

of agreement is good. The low-pass filtered results are shown in Fig. 18. Similar to the deck only case, the experimental and numerical forces are in good agreement except that the first upward vertical force is consistently underestimated by the numerical result.

Fig. 19 shows the close-ups of the numerical time series of the wave forces and the incident wave recorded at the focus point. Fig. 20 shows the evolution of the free-surface and the associated flow field pressure on a vertical sheet located at $y = -0.125B$, which is used here to correlate with the peak wave forces in Fig. 19. Without the contamination of structural resonance as occurred in the experiments, clear peaks are found in the numerical horizontal time series (see Fig. 19(a)). Each time the wave crest encounters an I-beam (or cross girder), a horizontal impulsive force is induced. As such, a total of 8 large peaks occur in the horizontal force time series, referred to as H1 to H8. Note that peak force H1 associated with the incident wave crest impinging on the front-face of the deck (including the first cross girder) is less obvious to see, since its time window overlaps partly with the occurrence of peak H2, which arises due to the interaction of the wave crest with the second cross girder. As the wave advances down the deck, the wave crest height becomes smaller from the first ceiling slab region towards the last ceiling slab region, due to the fact that wave energy is lost as momentum is transferred to the structure and the incident wave crest height decreases after the focus point. When the wave crest advances to the 6$^{\text{th}}$ ceiling slab region, it is unable to reach the underside of the deck until later it interacts with the 7$^{\text{th}}$ cross girder, and the same scenario is found in the 7$^{\text{th}}$ ceiling slab region. This leads to the fact that peaks H1, H7 and H8 are due to direct wave impingements on the cross girders. As will be shown later, peaks H2 to H6 are mainly caused by local high pressures associated with entrapped down-wave air-pockets formed by the wave crest and the structure. These wave-structure interactions can also be identified clearly in supplementary Movie 5.

In terms of vertical impulsive force, it can be seen from Fig. 19(b) that the vertical force is mainly induced when the wave crest impacts on the deck bottom (or the ceiling slabs in the grillage). In total 6 large peaks are found in the vertical force time series, referred to as V2 to V7. In contrast to the deck only case, there is no vertical peak force

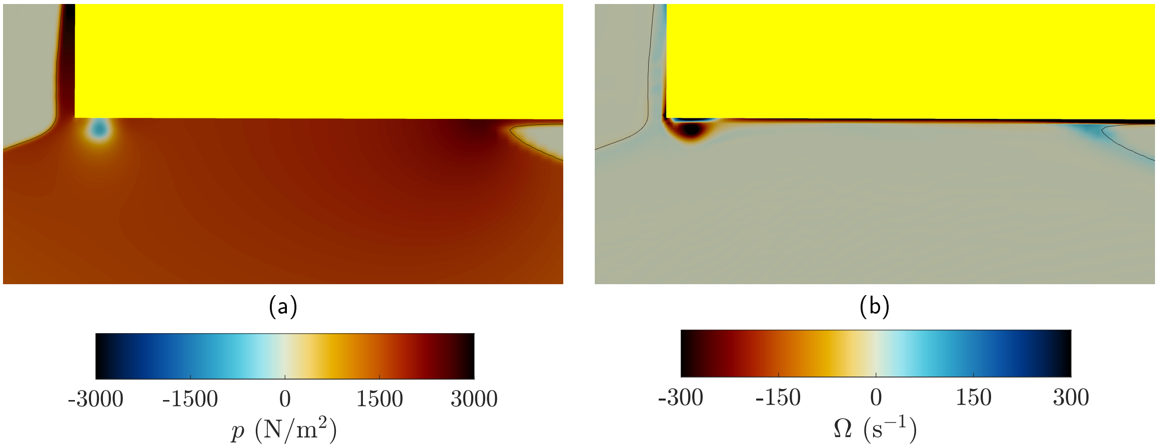

Fig. 15: Snapshots of (a) pressure and (b) vorticity contours in the mid-plane ($y = 0$) captured at $t = 0.08$ s. The outline of free-surface is denoted using solid black lines. The colour legend in (b) is such that red represents counterclockwise vorticitiy and blue represents clockwise vorticity (when looking into the paper).

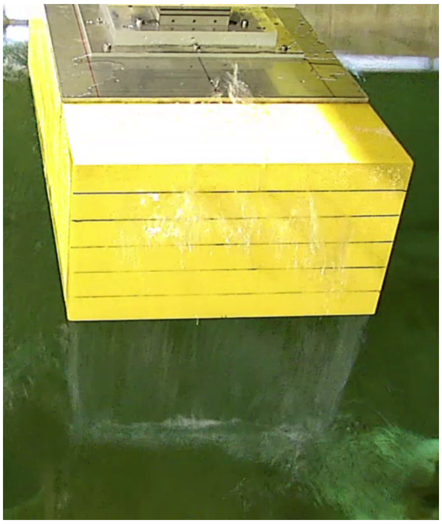

Fig. 16: Experimental snapshot of water-curtain on and below the front-face of deck.

induced by the initial interaction of the wave crest with the front-corner due to the presence of the I-beam ahead (i.e. the first cross girder), so there is no peak V1. Peaks V2 to V6 in the vertical force time series align well in time with peaks H2 to H6 in the horizontal force time series, both occurring during the wave-deck interactions in the 1$^{\text{st}}$ to 5$^{\text{th}}$ ceiling slab regions formed by the corresponding cross girders. In the 6$^{\text{th}}$ ceiling slab region, the wave crest impinges on the 7$^{\text{th}}$ cross girder before it runs up the cross girder to reach the underside of the deck (see Fig. 20(g) and (h), and supplementary Movie 5). As a result, peak H7 occurs slightly before peak V7.

Fig. 21 shows the velocity vector fields of the incident wave crest underneath the deck for cases without and with an I-beam grillage. For the case with a grillage, as the wave advances along the underside of the deck, the wave crest interacts with each cross girder in a similar fashion. Different from the case without a grillage where the velocity of the wave crest right underneath the deck remains almost horizontal from wave entry to wave exit, the velocity of wave crest for the case with a grillage appears to be more vertical and the water particles ‘leap’ towards the rectangular ceiling slab region ahead each time the wave crest is obstructed by an individual I-beam.

Fig. 22(a)-(f) show the interactions of the incident wave crest with the first ceiling slab region from the bottom view (see supplementary Movie 6 for full wave-deck interactions). Intercepted by the protruding I-beam at the front-face,

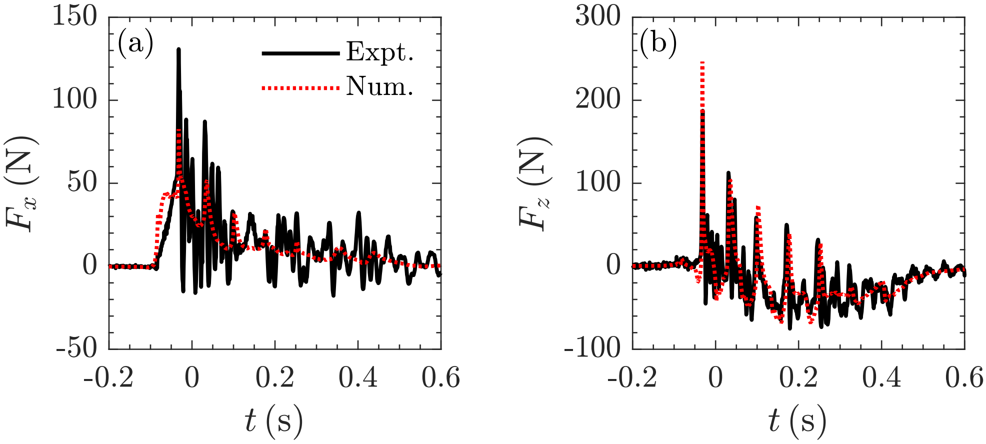

Fig. 17: Time series of (a) horizontal force and (b) vertical force on structure for solid deck with an I-beam grillage.

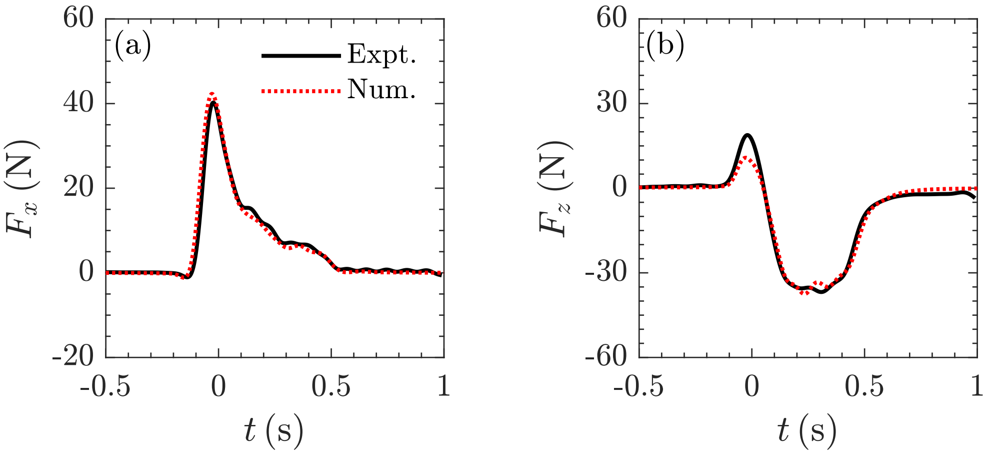

Fig. 18: Time series of low-pass filtered (a) horizontal force and (b) vertical force on structure for solid deck with an I-beam grillage. The cut-off frequency of low-pass filter is 9 Hz.

the wave crest slams upward towards the ceiling slab ahead. The initial impact area occurs near the middle part of the ceiling slab and rapidly extends mainly along the wave propagation direction as the wave crest advances down-wave. During the process, two air-pockets are trapped in the ceiling slab region – one formed by the wave crest, the ceiling slab and the up-wave cross girder, and the other formed by the wave crest, the ceiling slab and the down-wave cross girder, referred to as 'up-wave air-pocket' and 'down-wave air-pocket', respectively. Demarcated by the leading and trailing edges of the fully wetted area, three regions are defined in the ceiling slab region from up-wave to down-wave – an up-wave air-pocket region, a fully-wetted region and a down-wave air-pocket region, see Fig. 22(c).

Fig. 23 shows the evolution of pressure on the underside of the deck (see supplementary Movie 7 for full wave-deck interactions), corresponding to the time instants of Fig. 22. As a result of the complex wave-deck interactions associated with entrapped air-pockets, the pressure field becomes relatively less symmetric compared to the deck only case, although the geometry of the model and incident wave are symmetric with respect to the mid-plane (i.e. $y = 0$). As shown in Fig. 23(b) and (c), an initial negative pressure region is found corresponding to the up-wave air-pocket region due to the motion of the up-wave pocket driven by the wave crest. This leads to a sudden downward suction force and hence the set-down at $t = -0.040$ s prior to peak V2 in the vertical force time series, which also occurs in the second to fifth ceiling slab regions where apparent entrapped up-wave air-pockets are found (see the corresponding set-downs in Fig. 19). Associated with the fully-wetted region is a positive pressure region due to the direct impingement of the wave crest on the ceiling slab. As the wave crest advances closer towards the cross girder ahead, the positive pressure

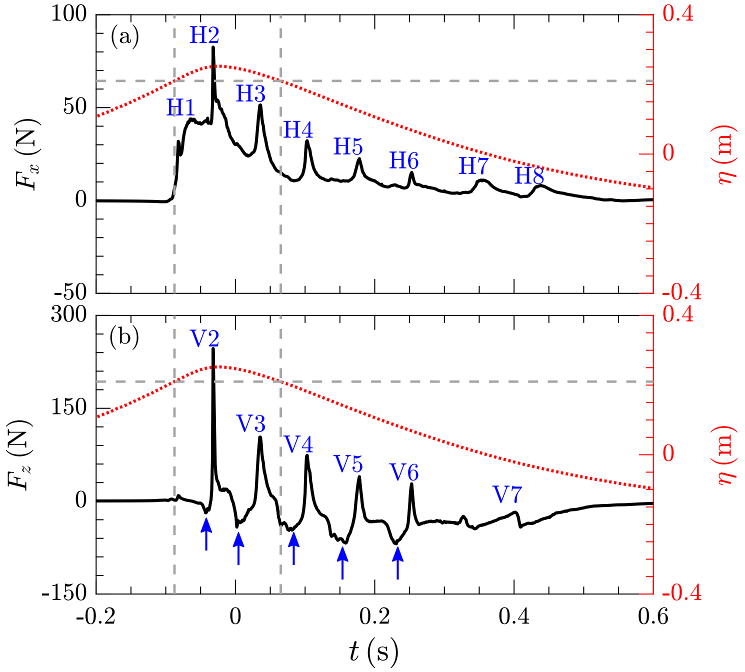

Fig. 19: Time series of numerical incident wave group and forces on structure for solid deck with an I-beam grillage. Solid black lines for (a) horizontal force (b) vertical force; dotted red line for incident wave;blue arrows indicate set-downs.

in the down-wave air-pocket region increases. At $t = -0.032$ s, the down-wave air-pocket is trapped in the grillage, inducing high pressures near the local impact zone with an almost semicircular front, as shown in Fig. 20(d). This corresponds to the occurrence of peak H2 and V2, which is more than 2 and 8 times the counterparts for the deck only case, respectively. The impulsive impact is so large that the negative pressure in the up-wave air-pocket region temporarily turns positive, see Fig. 23(d). Soon after the impulsive impact, the pressure in the up-wave air-pocket region turns negative again, see Fig. 23(e). Here we note that, for the other down-wave ceiling slab regions, the pressure in the up-wave air-pocket region is similar to that in the first ceiling slab region – the pressure always remains negative except when high local pressures are induced due to wave impingement associated with the entrapped down-wave air-pockets. As shown in Fig. 22(e), the entrapped down-wave air-pockets quickly collapse as the wave crest passes the cross girder ahead. Santo et al. (2020) reported that there was a loud boom sound each time the wave crest hit the bottom of deck with a grillage in the experiments. Presumably these sounds were caused by the rapid formation and collapse of the down-wave air-pockets, which not only increases the loads on the structure but also leads to stronger dynamic vibrations of the structure in the experiments. By contrast, the sound was much reduced in the deck only experiments where no such entrapped air-pockets are formed as observed in the NWT.

We note in passing that here our two-phase Navier-Stokes solver treats both water and air as incompressible, so any loss of wave energy in compression of the entrapped air-pockets is not considered. However, air compressibility should not have any significant influence on the overall forces on deck, as seen from the level of agreement between measured and numerical impact force time histories. Seiffert et al. (2015) demonstrated that the effect of air compressibility is not important for the overall forces on a bridge with underneath girders arising from solitary wave impact by solving both incompressible and compressible Euler's equations in two-dimensions. While in a 3D scenario, we expect the effect of air compressibility to be even smaller as the air can escape from the sides of the deck.

Triangularisation of the wetted area underneath the deck following the wave crest can be seen as the wave crest advances further down the underside of the deck at later time instants, but with a smaller rate of change compared to the deck only case, as shown in Fig. 22(g) and (h). The water on the ceiling slabs accelerates downwards and drops into the water below, inducing downward suction forces associated with the added mass effect, see Fig. 23(g) and (h).

Fig. 24 shows the time series of pressure calculated at the front-face and the ceiling slabs in the grillage. The sampling points at the front-face are 2 cm and 3 cm above the bottom of the I-beam grillage, so the points are on the

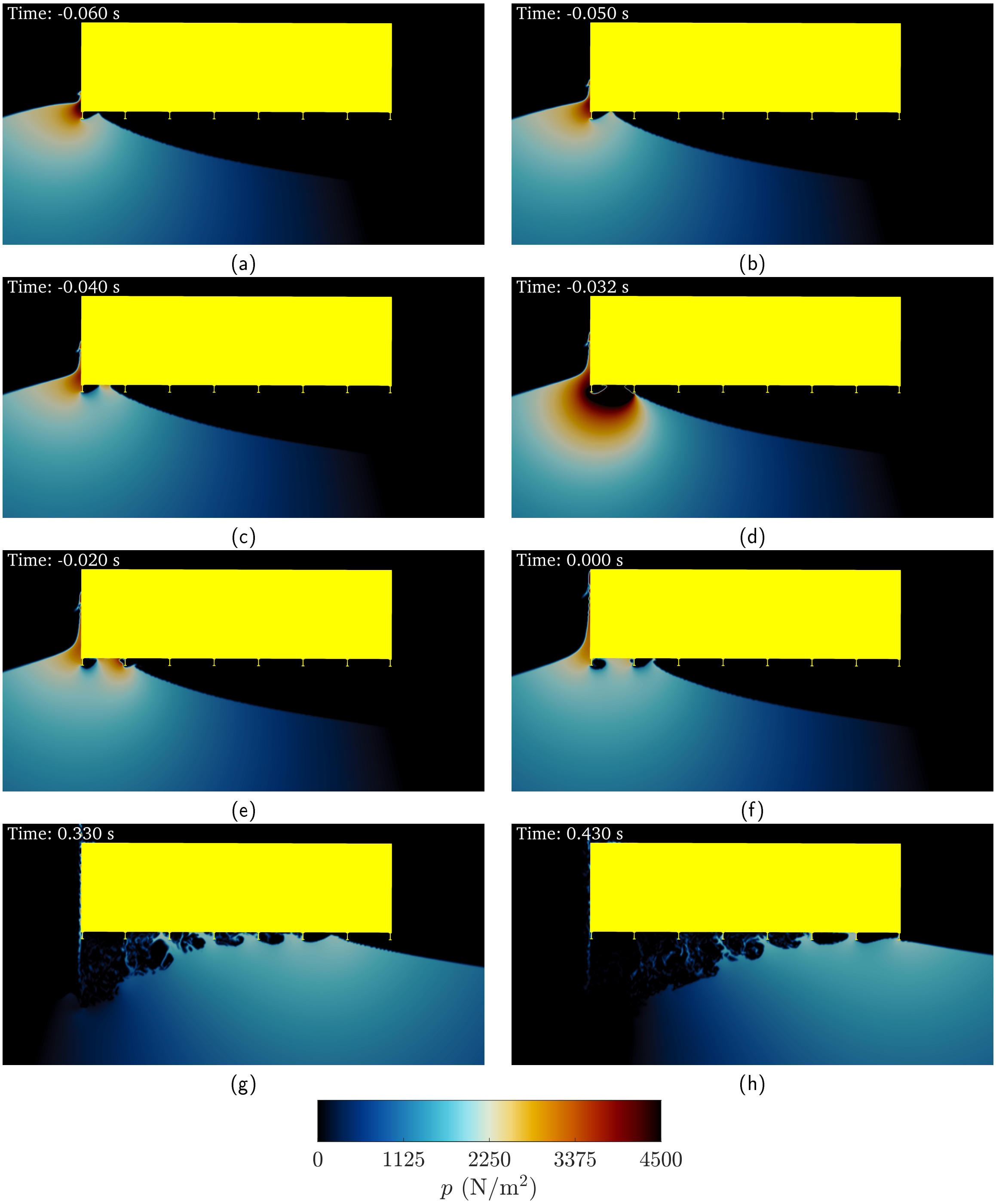

Fig. 20: Pressure of flow field from side view at $y = -0.125B$ for solid deck with an I-beam grillage.

front-face of the I-beam grillage and the front-face of the deck, respectively. Four pairs of sampling points are used to record the pressures on the first four ceiling slabs. Each pair consists of a point near the up-wave end and a point near the down-wave end of the ceiling slab. For instance, $x = 1.5$ cm and $x = 14$ cm are located in the first ceiling slab and are located near the ends of the first ceiling slab, which are within the regions of entrapped up-wave and down-wave air-pockets, respectively. When the entrapped down-wave air-pocket is formed in the first ceiling slab region (see Fig. 20(d)), the induced localised high pressure region not only causes large pressures in the down-wave air-pocket region,

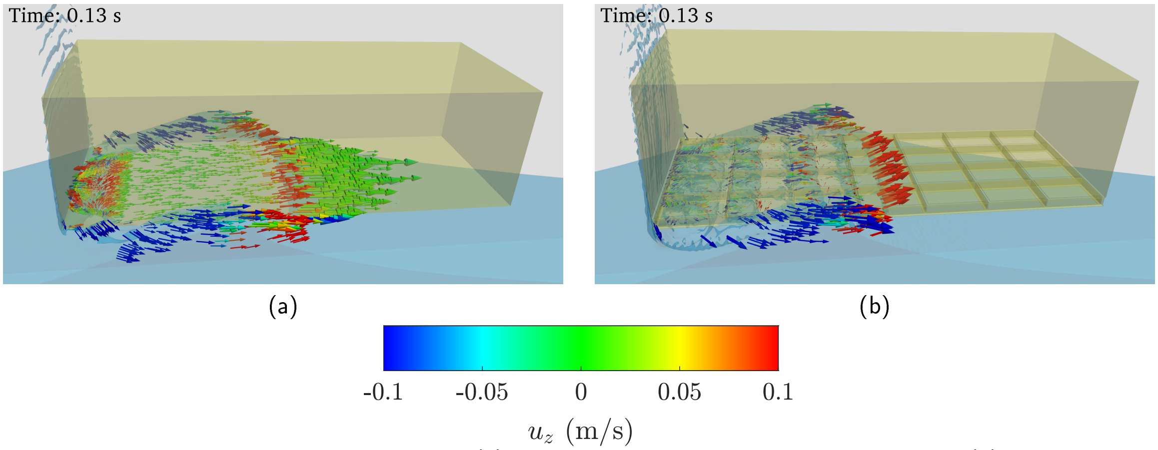

Fig. 21: Velocity vector underneath the deck for (a) solid deck without an I-beam grillage, and (b) solid deck with an I-beam grillage. The color bar is based on the magnitude of vertical velocity.

but also gives rise to the up-wave pressure field. Specifically, the negative pressure calculated at $x = 1.5$ cm in Fig. 24(b) is temporarily reversed to positive pressure, and a second peak is found in the time series of pressure calculated at the front-face as shown in Fig. 24(a), note the perfect alignment of the peaks at $t = -0.032$ s. Similar phenomena can be found for the other pressure time series as well but with decreased peak values of pressure with the sampling positions further away from the leading-edge of the deck. The presence of the down-wave air-pockets in the ceiling slab regions are responsible for the peaks of negative pressures recorded at $x = 14$ cm, $x = 29$ cm, etc.

Fig. 25 shows the longitudinal distribution of maximum positive and negative pressures along the deck bottom for both the deck only case and deck with I-beam grillage case. The pattern is simple for the deck only case. The maximum positive pressure generally decreases from the front-corner to the down-wave end, while the maximum negative pressure is largest near the front-corner and remains constant down the deck before slowly decreasing to zero near the down-wave end. For the deck with grillage case, 7 pairs of curves corresponding to the 7 ceiling slab regions are separated due to the presence of the I-beams. For each of the first five pairs of curves, there is a clear line of demarcation near the middle of the maximum positive and negative pressure curves in Fig. 25(b) where a sudden pressure jump can be found. The demarcation line roughly corresponds to the location where the up-wave and down-wave air-pockets are separated by the wave crest, see the illustration in the first ceiling slab region as shown in Fig. 25(a). The left (or up-wave) part of the maximum negative pressure is mainly determined by the entrapped up-wave air-pocket effect and the right (or down-wave) part of the maximum positive pressure is mainly determined by the entrapped down-wave air-pocket effect. Such a pattern is absent for the sixth and seventh pairs of curves as no entrapped up-wave and down-wave air-pockets are formed in the corresponding ceiling slabs.

6. Effect of air entrapment

As demonstrated in §5 for the deck with a grillage case B, the entrapment of up-wave air-pocket and the added mass effect (associated with water dropping away from the underside of the deck) contribute to the large downward vertical load on deck, while the entrapment of down-wave air-pocket is related to the localised high pressures in the grillage thus causing impulsive horizontal and upward vertical loads on deck. In the following subsections, the significance of entrapped air-pocket effects are investigated.

6.1. Effect of air entrapment on vertical wave-in-deck load

Here we attempt to evaluate the relative importance of the entrapped up-wave air-pocket effect and the added mass effect on downward vertical force on deck. Fig. 26 shows the comparison of vertical force power spectra between case A and case B. For case A the downward vertical force is mainly due to the added mass effect and the frequency zone of significance is lower than 3 Hz. While for case B obvious high-frequency components beyond 8.3 Hz are seen as well as similar low-frequency components as for case A. Based on this observation, it is plausible that the added mass effect is dominated by low-frequency components and the entrapped up-wave air-pocket effect is dominated by high-frequency components. The low- and high-frequency components of case B are separated using low- and high-pass

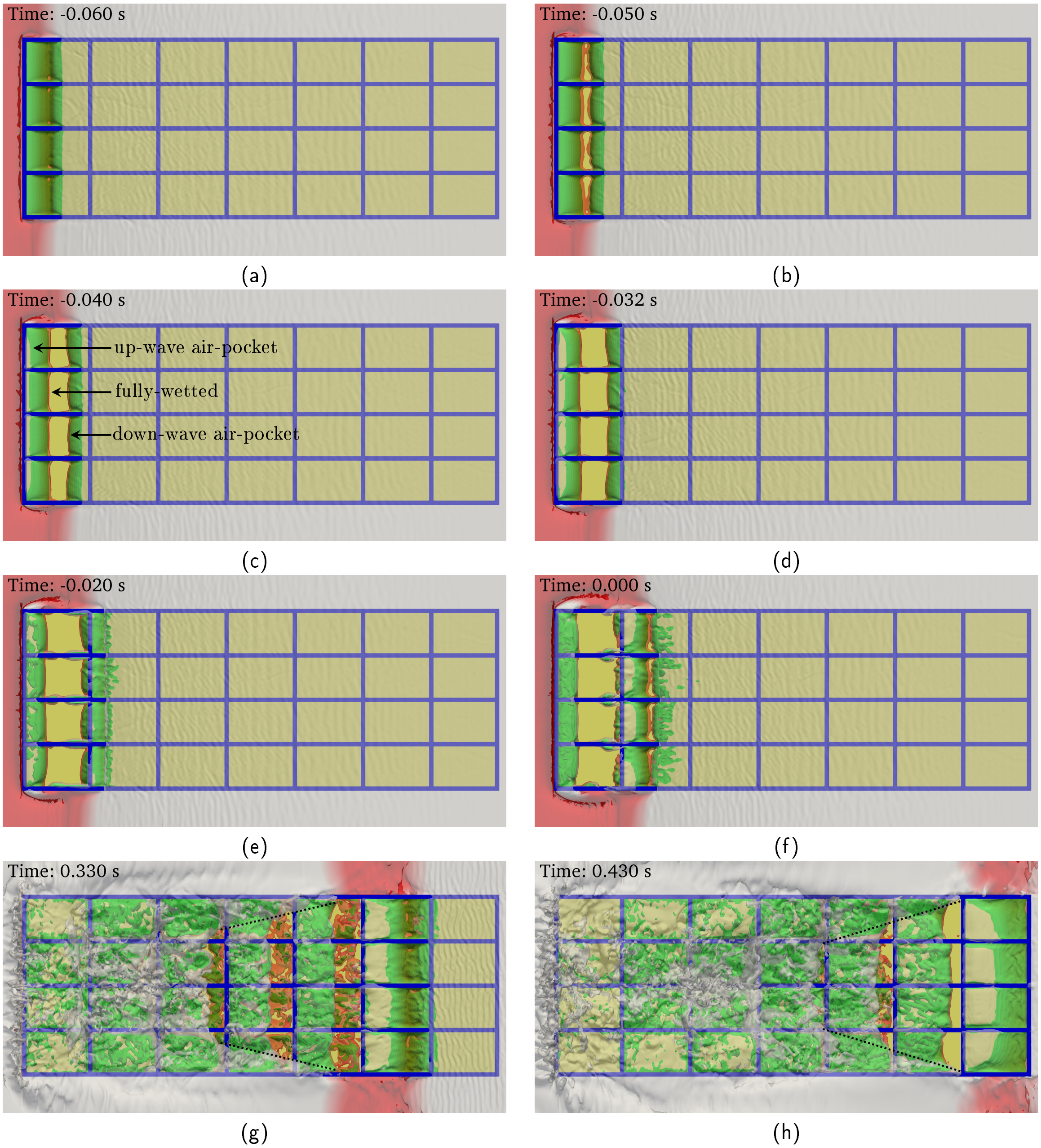

Fig. 22: Bottom view of wave-structure interaction for solid deck with an I-beam grillage. Red color and white color represent free-surface above ($z \geq s$) and below the deck bottom ($z < s$), respectively; green color represents air-pockets in the grillage ($s < z < s + I$), which are extracted by including cells with air volume of 95% to 99%; the exposed yellow region represents the fully-wetted area; the dotted black lines in (g) and (h) illustrate the triangularisation of the wetted area.

filters, respectively, with cut-off frequency of 8.3 Hz. The results are shown in Fig. 27, where the low- and high-pass vertical forces of case A are plotted in the same figure for comparison. It is found that the low-frequency downward vertical force due to the added mass effect for case B is roughly the same as that of case A. The high-frequency vertical force of case A remains close to zero during the downward force window ($t > 0.02$ s), except for a small kink at $t = 0.12$ s as a result of the impulsive force due to the wave-back leaving the front-face of deck; while the high-frequency vertical force of case B sees large upward and downward vertical forces related to the presence of entrapped down-wave and

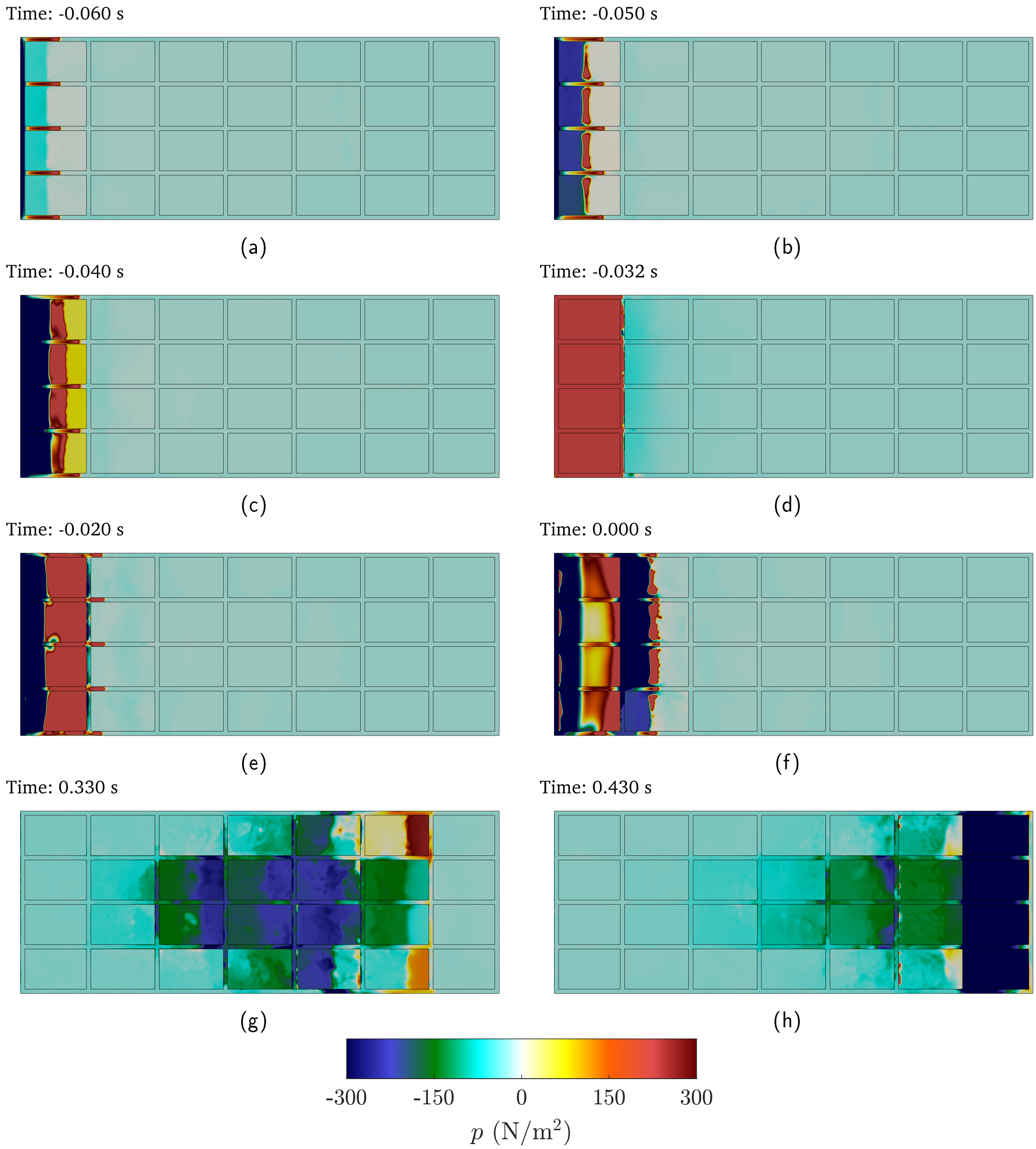

Fig. 23: Evolution of pressure on the underside of the deck for solid deck with an I-beam grillage.

up-wave air-pockets, respectively. In terms of the relative importance of the two factors, the downward vertical force due to the up-wave air-pocket effect is larger than that due to the added mass effect in the initial phase ($t < 0.09$ s), while the trend reverses after that. The set-down (i.e. high-pass downward vertical peak force) increases from the first ($t = -0.04$ s) to the second ($t = 0$ s), since the first set-down is only related to one entrapped up-wave air-pocket in the first ceiling slab region while the second set-down is related to two entrapped up-wave pockets in both the first and second ceiling slab regions (see Fig. 20(f), Fig. 22(f) and Fig. 23(f)). Thereafter, the set-down decreases in general as a result of wave energy loss during wave-deck interactions. Due to the combined contribution of entrapped up-wave air-pocket and added mass effects, the total downward vertical force is much larger than that for the solid deck only, e.g. the largest set-down of case B is approximately twice the largest downward vertical force of case A (see Fig. 5 and Fig. 17).

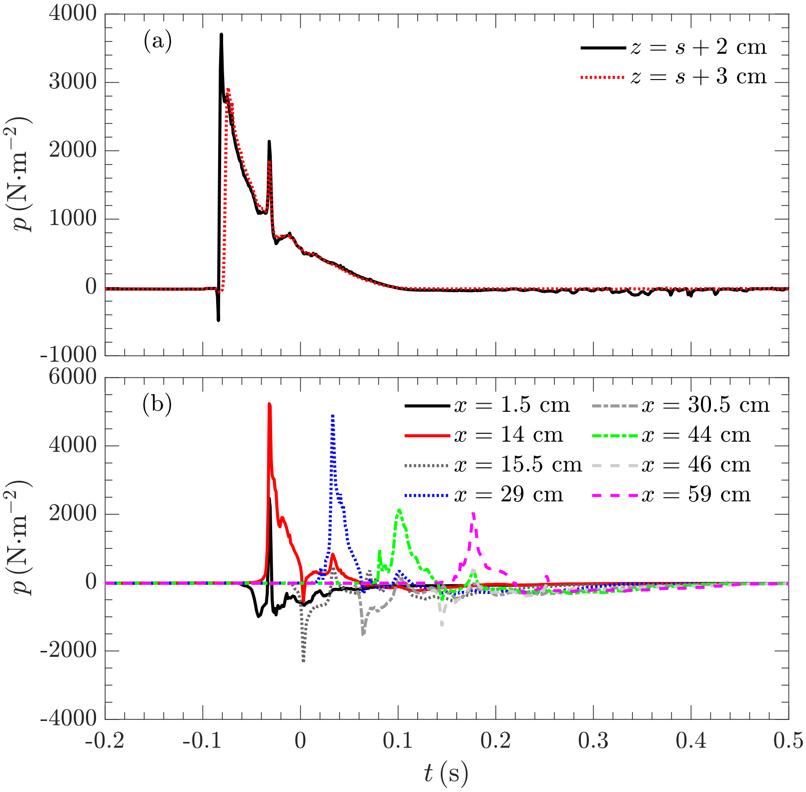

Fig. 24: Time series of pressure calculated at the deck (a) front-face and (b) bottom for the solid deck with grillage case. The vertical sampling positions in (a) are 2 cm and 3 cm above the deck bottom; the longitudinal sampling positions in (b) are the distance down-wave from the front-face; the transverse position of the sampling points is $y = 1$ cm.

6.2. Effect of air entrapment on horizontal wave-in-deck load

To investigate the effect of air entrapment in the grillage on the horizontal load on deck, a hollowed-out deck with a grillage beneath is considered (see Fig. 28, referred to as 'case C'). Compared with the deck with a grillage case B in §5, the ceiling slabs between cross girders and their above deck block are removed so that the eight cross girders along the wave propagation direction extend vertically up as dividing walls to provide the same inundation as cases A and B. The full wave-structure interaction is shown in Movie 8 available at xxxx.

Fig. 29 shows the comparison of numerical time series of horizontal force for the deck with a grillage case B and hollowed-out deck with a grillage case C, each of which sees eight peaks (the first to eight peaks of case C are referred to as h1 to h8, respectively). For the deck with a grillage case B, peaks H1, H7 and H8 are due to direct wave impingements on the cross girders, while peaks H2 to H6 are associated with entrapped down-wave air-pockets. For the hollowed-out deck with a grillage case C, no down-wave air-pocket regions are formed due to the absence of ceiling slabs, so peaks h1 to h8 are all due to direct wave impingements on the eight cross girders. As a result, peaks h1, h7 and h8 of case C align well in time with peaks H1, H7 and H8 of case B, respectively, while peaks h2 to h6 of case C appear later in time than the counterparts of case B. This also renders the first peak of case C easier to identify than case B. In terms of amplitude, the first peaks of the two cases are almost the same during the rise time (defined as the period from the initial increase to the peak of the impulse) as the initial wave impingements on the front-face of deck are almost the same. Peak h2 of case C is approximately 25% smaller than peak H2 of case B despite case C having a larger inundation and hence impact area with the second cross girder and dividing wall, demonstrating the importance of entrapped down-wave air-pockets formed in the grillage on the horizontal wave-in-deck load. For case C, peak h2 is larger than peak h1 even after energy loss during the initial wave impingement on the front-face of deck. This suggests that the 'leaping' motion of the wave crest obstructed by the first I-beam (or front-face of deck) is also important to the large amplitude of the second peak. Peaks h3 to h6 of case C are larger than the counterparts of case B, indicating that

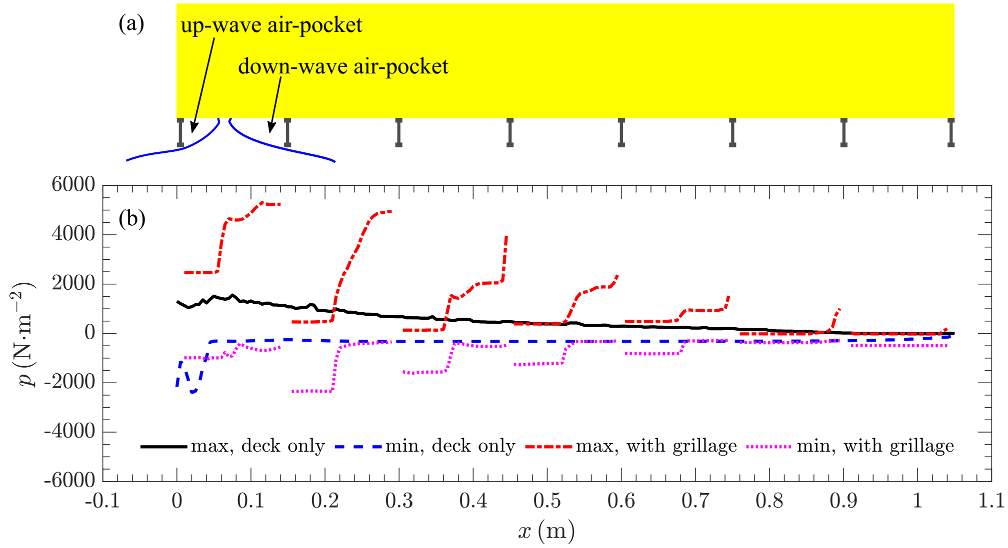

Fig. 25: Longitudinal distribution of maximum positive and negative pressures along the deck bottom. The transverse position of the sampling points is $y = 1$ cm. (a) provides an illustration of the deck with I-beam grillage and entrapped up-wave and down-wave air-pockets in the first ceiling slab region, where the longitudinal position is related to that in (b). In (b), the solid black and dashed blue lines represent the maximum positive and negative pressure distributions for the deck only case, respectively; the dash-dotted red and dotted magenta lines represent the maximum positive and negative pressure distributions for the deck with I-beam grillage case, respectively.

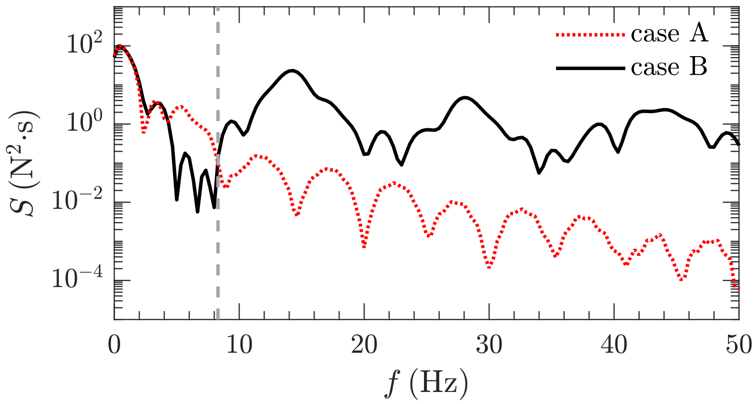

Fig. 26: Comparison of vertical force power spectra for numerical case A (deck only) and case B (deck with an grillage).

more wave energy is lost when down-wave entrapped air-pockets are formed in the grillage during wave impingements on the cross girders. From Fig. 27 and Fig. 29, it appears that entrapped air-pockets are more important for vertical force than horizontal force, presumably due to the way the wave crest interacts with each I-beam cross girder.

7. Conclusions

In this work the experiments of three-dimensional (3D) wave-in-deck loads on a solid deck with and without an I-beam grillage beneath have been reproduced in a numerical wave tank by solving numerical solutions of the Navier-Stokes equations with a volume of fluid method. A non-breaking transient focused wave group is used to impinge on the front-face of the deck, so the entire complex wave-structure interaction can be simulated with only one large wave event interacting with the deck. The correlations between force variation and flow field information in high spatial

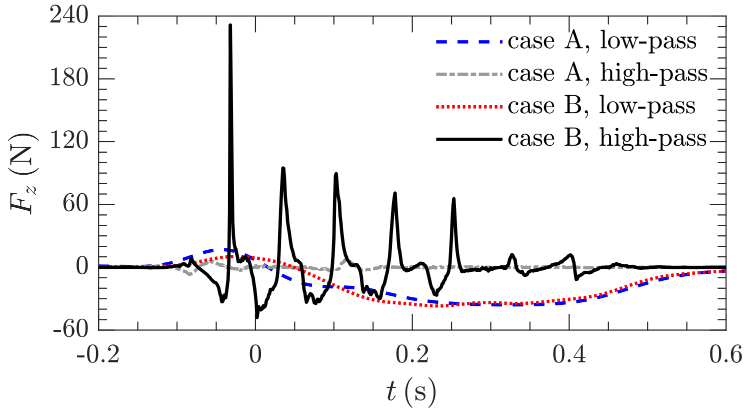

Fig. 27: Low-pass and high-pass vertical force components for numerical case A (deck only) and case B (deck with an grillage). The cut-off frequency of filters is 8.3 Hz as indicated using a dashed grey line in Fig. 26.

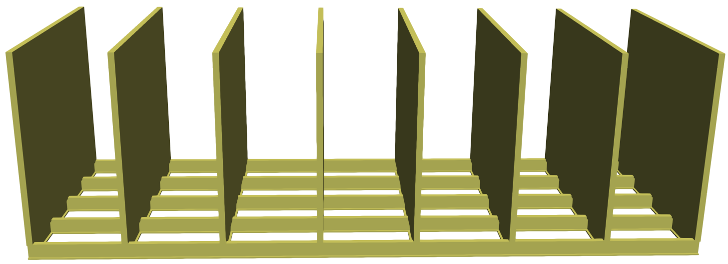

Fig. 28: Illustration of a hollowed-out deck with an I-beam grillage and vertical dividing walls only.

and temporal resolution have been successfully established to gain physical insights into the wave-deck interactions, extending the experimental study by Santo et al. (2020).

The wave-in-deck loads on a solid deck are relatively simple. The 3D horizontal force, characterised by a single peak in time, is close to 2D. In contrast, the vertical force time-history is more complex, consisting of an upward force and downward suction force, with a secondary upward kink during the suction force. The kink is a robust feature and is related to the back-face of the incident wave dropping below the front-edge of the deck and rapidly followed by a local close to impulsive force on the bottom of the deck just beyond the edge. The downward suction force is dominated by the added mass effect associated with triangularisation of the wetted area underneath the deck, which is a 3D effect and therefore any 2D simulation will overpredict the vertical wave-in-deck loads. The mismatch of maximum inundation level and maximum horizontal force in time provides evidence that the horizontal force is not solely dependent on the inundation level; the crest shape and associated velocity profile underneath the crest are also important.

The wave-in-deck loads on the solid deck with an I-beam grillage beneath, on the other hand, are more complicated, with successive force spikes observed for both the horizontal and vertical loads. From the flow visualisation, evidence of entrapped up-wave and down-wave air-pockets within the ceiling slab regions of the grillage is presented, and when the wave crests interact with the deck, upward leaping motions of water into the entrapped air-pockets are observed within the grillage. Localised high positive pressures are induced when down-wave air-pockets are entrapped in the grillage, leading to a series of large upward vertical impulsive forces. The pressure pulses are so large that they can give rise to the up-wave pressure field causing a second peak in the pressure time series, and even temporarily reverse the negative pressures on the ceiling slabs to positive. It is found that both the local high pressures associated with the down-wave air-pocket effect and the upward jetting motion of wave crest contribute to a series of large horizontal impulsive forces.

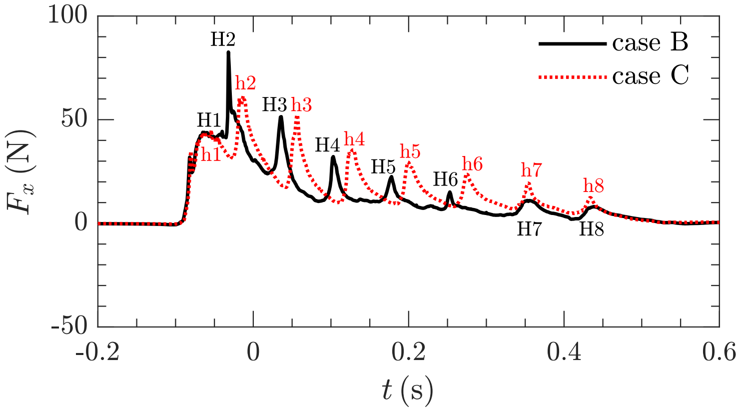

Fig. 29: Time series of numerical horizontal forces on solid deck with an I-beam grillage (case B) and hollowed-out deck with an I-beam grillage (case C).

In contrast to the deck only case, both high-frequency up-wave air-pocket effect and low-frequency added mass effect are important for the downward suction force on the solid deck with a grillage. The combined effects of the two factors lead to much larger downward vertical forces than the deck only case. Typically, the up-wave air-pocket effect dominates the initial phase of the downward vertical force, whereas the trend reverses at later times as the wave exits the deck and wave energy is lost during wave-deck interactions. The entrapped air-pocket effects are found to be more important for the vertical forces than for the horizontal forces. Overall, this study highlights the importance of 3D effects to be considered for violent wave-in-deck associated with overturning/breaking waves, wherein entrapped air-pockets/entrained air bubbles are easily found.

Although air compressibility is not considered in this study, it seems not to have any significant influence on the global forces on deck at the model scale (Seiffert et al., 2015). In a full-scale scenario, however, compressibility of entrapped air-pockets and/or entrained air bubbles may have a larger effect on the scaling of both local pressures and global forces, and how the scaled pressures and forces compare with the Froude law scaling remains a fascinating, complex and important question. On one hand, air compressibility may have a larger 'cushioning' effect at the full-scale – some of the wave energy is lost in compressing or stretching the entrapped air-pockets in the grillage (Cuomo et al., 2009, 2010), and the likely increase of entrained air for increased scale may reduce the full-scale impact pressures to values below the Froude scaling values (Bredmose et al., 2015), so direct Froude scaling from the model scale to the full-scale might significantly over-predict the wave impact pressures. On the other hand, the results of Bredmose et al. (2015) indicated that Froude scaling might significantly underpredict pressures and forces due to the presence of entrapped air-pockets. Therefore, further investigation of air compressibility at the full-scale and how the impact pressures and forces scale would be interesting.

Despite the limited cases investigated in this study, it is believed that the general physics of wave-deck interactions should be similar for other non-breaking waves. For breaking waves, the horizontal impulsive impact at the front-face of deck during wave entry can be much larger than the cases considered in this study and air dynamics must be accounted for to properly resolve local pressures. In addition, for wave-in-deck loads under oblique waves and with the presence of a jacket underneath the deck, the wave-structure interactions may be different. We leave investigation of these additional complications for future work.

CRediT authorship contribution statement

Hongchao Wang: Conceptualization, Methodology, Software, Validation, Formal analysis, Writing - original draft, Visualization. **H. Santo:** Conceptualization, Methodology, Formal analysis, Writing - review & editing. **P.H. Taylor:** Conceptualization, Methodology, Formal analysis, Writing - review & editing. **S.S. Dai:** Resources, Writing - review & editing. **A.H. Day:** Resources, Writing - review & editing. **E.S. Chan:** Writing - review & editing, Project administration, Funding acquisition.

Table 1
List of mesh details. Δx_1 is the upstream streamwise (i.e. along the wave propagation direction) mesh size; Δx_2 is the streamwise mesh size near the deck, refined from $x = \pm 0.3L$ towards the front-face of the deck ($x = 0$); Δz is the vertical mesh size near the free-surface; Δy is the transverse (i.e. perpendicular to the wave propagation direction) mesh size.

Label	Dimension	Total cell number (million)	Δx_1 (cm)	Δx_2 (cm)	Δz (cm)	Δy (cm)
mesh M1	2D	0.024	3	3	3	N/A
mesh M2	2D	0.431	1	1 − 0.25	0.25	N/A
mesh M3	2D	0.816	1	1 − 0.125	0.125	N/A
mesh M4	3D	23.0	1	1 − 0.25	0.25	2.5
mesh M5	3D	67.9	1	1 − 0.25	0.25	0.75
mesh M6	3D	95.7	1	1 − 0.25	0.25	0.25
mesh M7	3D	3.7	3	3	3	0.75
mesh M8	3D	129.1	1	1 − 0.125	0.125	0.75

Declaration of competing interest

The authors declare that they have no known competing financial interests or personal relationships that could have appeared to influence the work reported in this paper.

Acknowledgement

We acknowledge the support from Singapore Maritime Institute (SMI) through project ID SMI-2015-OF-12 to National University of Singapore where the earlier part of the work was conducted, and A∗STAR Science and Engineering Research Council, Singapore through grant number 172 19 00089 under the Marine & Offshore Strategic Research Programme (M&O SRP) to TCOMS where the latter part of the work was completed. The significant computing required for this work was performed on resources at the National Supercomputing Centre, Singapore (`https://www.nscc.sg`).

Appendix A Mesh independence study

A mesh independence study was carried out first to ensure that no obvious numerical dissipation occurs as the incident wave propagates along the NWT. From Wang et al. (2019), 200 cells per peak wave length and 50 cells per wave height works well in re-creating focused wave groups with wave steepness $k_z A_1 < 0.21$. However, a finer mesh is required to capture high-frequency wave components which become important in determining the crest amplitude for a more nonlinear wave with large wave steepness ($k_z A_1 = 0.28$). Three meshes M1, M2 and M3 with mesh details listed in Table 1 were used to re-create the experimental incident wave group. The obtained wave signals recorded at the focus point in the NWT are compared in Fig. 30. It is found that mesh M2 and mesh M3 agree well with each other, exhibiting 7% and 5% difference of inundation with the experimental data, respectively; while the coarse mesh M1 shows a much larger discrepancy (47%) with the experimental data, and no improvement was found with more iterations employed. Therefore, mesh M2 was adopted for wave generation, with approximately 550 cells per wavelength and 200 cells per nominal wave height ($2A$) were used.

2D simulations with the deck in place were then carried out with the same mesh M1, M2 and M3 to establish the quality of the simulated impact forces. Given the highly transient and nonlinear nature of wave-deck interactions, mesh M2 and M3 are in good agreement whereas mesh M1 exhibits large discrepancies compared to the other two meshes. Subsequently, to investigate the dependence of loads on transverse mesh resolution, 3D simulations were carried out for three additional meshes M4, M5 and M6 with three different transverse mesh sizes (see Table 1), while the longitudinal mesh size is based on mesh M2. As shown in Fig. 31, all three meshes agree reasonably well with each other in general. Compared to the fine mesh M6, mesh M5 shows 6% difference for the horizontal peak force and 3% difference for the first upward vertical peak force, while the counterpart differences are 15% and 7% for the coarse mesh M4. A further comparison is made in Fig. 32 among meshes M7, M5 and M8, which are the 3D counterparts of the 2D meshes M1, M2 and M3, respectively. The medium mesh M5 agrees well with the fine mesh M8 with respect to both horizontal and vertical loads on deck, whereas the coarse mesh M7 shows obvious discrepancies compared to the fine mesh. Therefore, mesh M5 is chosen as the optimum mesh size.

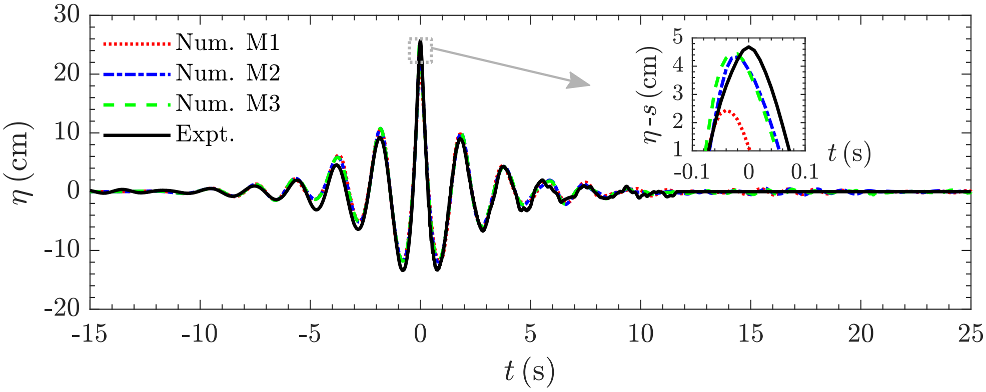

Fig. 30: Re-created incident wave groups with different meshes. 'Expt.' and 'Num.' stand for 'Experimental' and 'Numerical', respectively. In the close-up, $\eta - s$ represents the wave crest above the deck bottom.

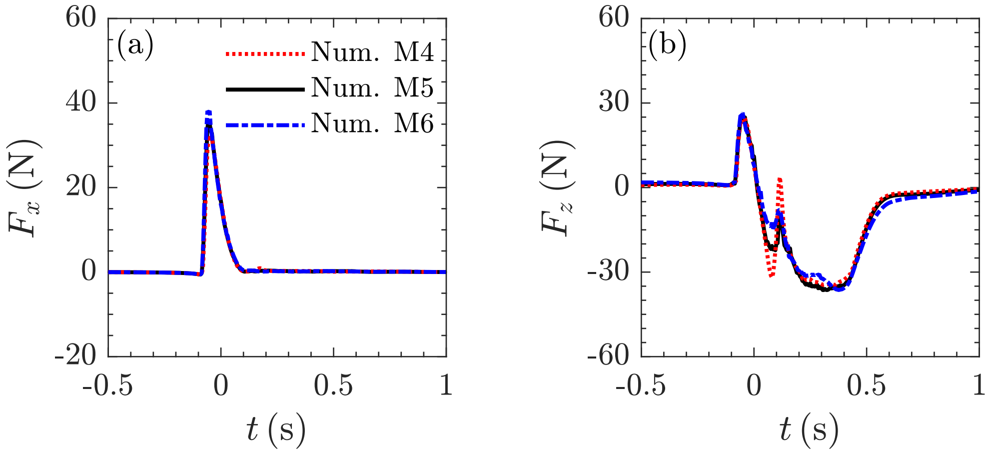

Fig. 31: Dependence of 3D wave-in-deck loads on transverse mesh resolution

Appendix B 2D simulation of wave-in-deck loads on a solid deck

A 2D simulation was carried out to investigate whether 3D effects are important for wave-in-deck loads on a solid deck. The simulation has a longitudinal slice of the 3D deck model with a configuration otherwise the same as the 3D simulation case A in §4, so it is equivalent to the deck spanning the entire width of the wave tank. The horizontal and vertical wave-in-deck loads are compared with the 3D results of case A in Fig. 33. It is found that 3D effects are negligible for the horizontal wave-in-deck force with the 2D horizontal force agreeing well with the 3D result. In contrast, 3D effects are obvious for the vertical wave-in-deck force. The 2D vertical force is much larger than the 3D result especially for the downward suction force during wave propagation stage underneath the deck. This is consistent with the added mass effect of dropping water from deck bottom, i.e. triangularisation of wetted area underneath the deck is observed in 3D which is absent in 2D.

References

Abdussamie, N., Ojeda, R., Thomas, G., Amin, W., 2017. Measurements of global and local effects of wave impact on a fixed platform deck. Proceedings of the Institution of Mechanical Engineers, Part M: Journal of Engineering for the Maritime Environment 231, 212–233.

API, 2014. Structural integrity management of fixed offshore structures. American Petroleum Institute (API), Washington DC .

Azadbakht, M., Yim, S.C., 2016. Effect of trapped air on wave forces on coastal bridge superstructures. Journal of Ocean Engineering and Marine Energy 2, 139–158.

Baarholm, R., 2005. A simple numerical method for evaluation of water impact loads on decks of large-volume offshore platforms, in: ASME 2005 24th International Conference on Offshore Mechanics and Arctic Engineering, American Society of Mechanical Engineers Digital Collection.

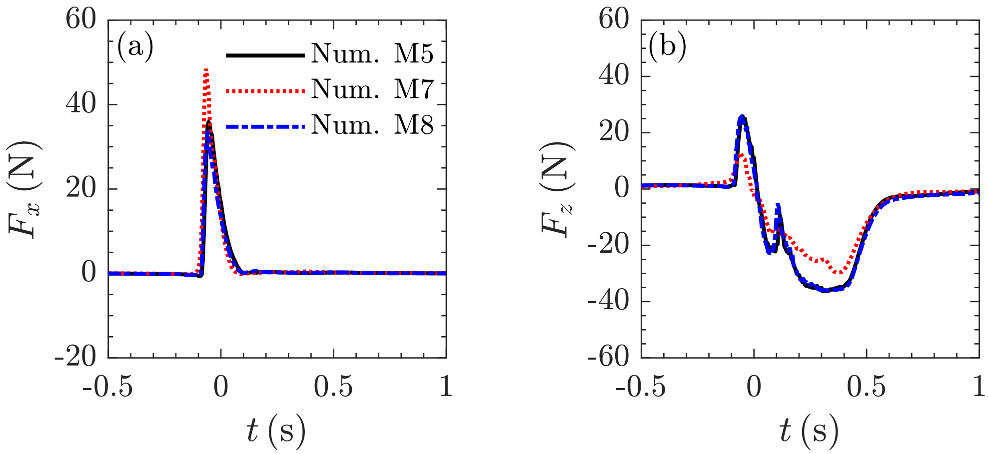

Fig. 32: Wave-in-deck loads in 3D with different meshes.

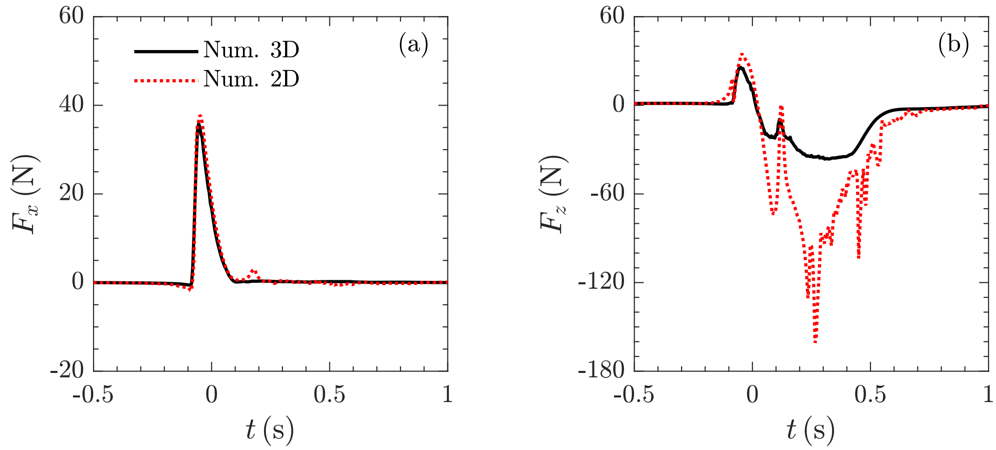

Fig. 33: Comparison of 2D and 3D numerical results of (a) horizontal force and (b) vertical force on a soild deck.

pp. 203–211.

Baarholm, R., 2009. Experimental and theoretical study of three-dimensional effects on vertical wave-in-deck forces, in: ASME 2009 28th International Conference on Ocean, Offshore and Arctic Engineering, American Society of Mechanical Engineers Digital Collection. pp. 451–459.

Berberović, E., van Hinsberg, N.P., Jakirlić, S., Roisman, I.V., Tropea, C., 2009. Drop impact onto a liquid layer of finite thickness: Dynamics of the cavity evolution. Physical Review E 79, 036306.

Bredmose, H., Bullock, G.N., Hogg, A.J., 2015. Violent breaking wave impacts. Part 3. effects of scale and aeration. Journal of Fluid Mechanics 765, 82–113.

Bredmose, H., Peregrine, D.H., Bullock, G.N., 2009. Violent breaking wave impacts. Part 2: modelling the effect of air. Journal of Fluid Mechanics 641, 389.

Chan, E.S., Melville, W.K., 1989. Plunging wave forces on surface-piercing structures. Journal of Offshore Mechanics and Arctic Engineering 111, 92–100.

Chen, Y., Wu, Y., Bahuguni, A., Gullman-Strand, J., Lv, X., Lou, J., Ren, W., 2018. Directional wave-in-deck loading on offshore structures with porous and plated decks with supporting i-beams. Coastal Engineering 137, 79–91.

Cuomo, G., Allsop, W., Takahashi, S., 2010. Scaling wave impact pressures on vertical walls. Coastal Engineering 57, 604–609.

Cuomo, G., Shimosako, K., Takahashi, S., 2009. Wave-in-deck loads on coastal bridges and the role of air. Coastal Engineering 56, 793–809.

Dias, F., Ghidaglia, J.M., 2018. Slamming: Recent progress in the evaluation of impact pressures. Annual Review of Fluid Mechanics 50, 243–273.

DNV-GL, 2019. Recommended practice DNVGL-RP-C205: Environmental conditions and environmental loads. DNV-GL, Norway .

Duong, T.T., Jung, K.H., Lee, G.N., Kim, H.J., Park, S.B., Shin, S., Lee, J., Suh, S.B., 2022. Pressure estimation of wave-in-deck loading using velocity fields obtained by particle image velocimetry. Ocean Engineering 257, 111581.

Duong, T.T., Jung, K.H., Lee, G.N., Park, H.J., Lee, J., Suh, S.B., 2021. Experimental study on wave-in-deck loading under focused wave conditions. Ocean Engineering 242, 110146.

Faltinsen, O.M., Timokha, A.N., 2009. Sloshing. Cambridge University Press.

Fang, Q., Liu, J., Hong, R., Guo, A., Li, H., 2021. Experimental investigation of focused wave action on coastal bridges with box girder. Coastal Engineering 165, 103857.

Hattori, M., Arami, A., Yui, T., 1994. Wave impact pressure on vertical walls under breaking waves of various types. Coastal Engineering 22, 79–114.

Hayatdavoodi, M., Seiffert, B., Ertekin, R.C., 2014. Experiments and computations of solitary-wave forces on a coastal-bridge deck. Part II: Deck with girders. Coastal Engineering 88, 210–228.

Jacobsen, N.G., Fuhrman, D.R., Fredsøe, J., 2012. A wave generation toolbox for the open-source CFD library: OpenFoam®. Intl. J. Numer. Meth. Fluids 70, 1073–1088.

Kaplan, P., 1992. Wave impact forces on offshore structures: re-examination and new interpretations, in: Offshore Technology Conference, Offshore Technology Conference.

Kaplan, P., Murray, J.J., Yu, W.C., 1995. Theoretical analysis of wave impact forces on platform deck structures. Technical Report. American Society of Mechanical Engineers, New York, NY (United States).

Kendon, T.E., Pakozdi, C., Baarholm, R.J., Berthelsen, P.A., Stansberg, C.T., Enger, S., 2010. Wave-in-deck impact: comparing CFD, simple methods, and model tests, in: ASME 2010 29th International Conference on Ocean, Offshore and Arctic Engineering, American Society of Mechanical Engineers Digital Collection. pp. 495–509.

Lind, S., Stansby, P., Rogers, B., Lloyd, P., 2015. Numerical predictions of water–air wave slam using incompressible–compressible smoothed particle hydrodynamics. Applied Ocean Research 49, 57–71.

Liu, S., Gatin, I., Obhrai, C., Ong, M.C., Jasak, H., 2019. CFD simulations of violent breaking wave impacts on a vertical wall using a two-phase compressible solver. Coastal Engineering 154, 103564.

Liu, Z., Guo, A., Liu, J., Fang, Q., 2022. Experimental investigation of loads of coastal bridge deck under the combined action of extreme winds and waves. Ocean Engineering 252, 111225.

Ma, L., Swan, C., 2020a. The effective prediction of wave-in-deck loads. Journal of Fluids and Structures 95, 102987.

Ma, L., Swan, C., 2020b. An experimental study of wave-in-deck loading and its dependence on the properties of the incident waves. Journal of Fluids and Structures 92, 102784.

Morison, J.R., Johnson, J.W., Schaaf, S.A., 1950. The force exerted by surface waves on piles. Journal of Petroleum Technology 2, 149–154.

Naess, A., Gaidai, O., 2011. Extreme value statistics of non-Gaussian random wave fields and the airgap problem for offshore platforms, in: Proceedings of the 8th International Conference on Structural Dynamics, Leuven, Belgium.

Park, H., Tomiczek, T., Cox, D.T., van de Lindt, J.W., Lomonaco, P., 2017. Experimental modeling of horizontal and vertical wave forces on an elevated coastal structure. Coastal Engineering 128, 58–74.

Peregrine, D.H., Thais, L., 1996. The effect of entrained air in violent water wave impacts. Journal of Fluid Mechanics 325, 377–397.

Santo, H., Taylor, P.H., Dai, S.S., Day, A.H., Chan, E.S., 2020. Wave-in-deck experiments with focussed waves into a solid deck. Journal of Fluids and Structures 98, 103139.

Scharnke, J., Lindeboom, R., Duz, B., 2017. Wave-in-deck impact loads in relation with wave kinematics, in: ASME 2017 36th International Conference on Ocean, Offshore and Arctic Engineering, American Society of Mechanical Engineers Digital Collection.

Seiffert, B.R., Ertekin, R.C., Robertson, I.N., 2015. Wave loads on a coastal bridge deck and the role of entrapped air. Applied Ocean Research 53, 91–106.

Sivagamasundari, V., Sannasiraj, S., 2020. Experimental study of vertical wave-in-deck force and pressure on a thin plate due to regular and focused waves. Journal of Ocean Engineering and Marine Energy 6, 199–210.

Sun, P.N., Luo, M., Le Touzé, D., Zhang, A.M., 2019. The suction effect during freak wave slamming on a fixed platform deck: Smoothed particle hydrodynamics simulation and experimental study. Physics of Fluids 31, 117108.

Teufel, L.W., Rhett, D.W., Farrell, H.E., 1991. Effect of reservoir depletion and pore pressure drawdown on in situ stress and deformation in the Ekofisk field, North Sea, in: The 32nd US Symposium on Rock Mechanics (USRMS), American Rock Mechanics Association.

Tromans, P.S., Anaturk, A.R., Hagemeijer, P., 1991. A new model for the kinematics of large ocean waves-application as a design wave, in: The First International Offshore and Polar Engineering Conference, August 11-16, Edinburgh, The United Kingdom.

Vyzikas, T., Stagonas, D., Buldakov, E., Greaves, D., 2015. Efficient numerical modelling of focused wave groups for freak wave generation, in: The Twenty-fifth International Ocean and Polar Engineering Conference, International Society of Offshore and Polar Engineers.

Wagner, H., 1932. Über stoß-und gleitvorgänge an der oberfläche von flüssigkeiten. ZAMM-Journal of Applied Mathematics and Mechanics/Zeitschrift für Angewandte Mathematik und Mechanik 12, 193–215.

Wang, H., Draper, S., Zhao, W., Wolgamot, H.A., Cheng, L., 2018. Development of a computational fluid dynamics model to simulate three-dimensional gap resonance driven by surface waves. Journal of Offshore Mechanics and Arctic Engineering 140.

Wang, H., Wolgamot, H.A., Draper, S., Zhao, W., Taylor, P.H., Cheng, L., 2019. Resolving wave and laminar boundary layer scales for gap resonance problems. Journal of Fluid Mechanics 866, 759–775.

Wen, B., Qu, K., Lan, G., Sun, W., Yao, Y., Deng, B., Jiang, C., 2022. Numerical study on hydrodynamic characteristics of coastal bridge deck under joint action of regular waves and wind. Ocean Engineering 245, 110450.

Wu, Y.L., Stewart, G., Chen, Y., Gullman-Strand, J., Lv, X., Kumar, P., 2016. A CFD application of NewWave theory to wave-in-deck simulation. International Journal of Computational Methods 13, 1640014.